# Continuous-wave Diode Pumping and Pulsed Operation of Alexandrite Lasers near 760 nm and $Tm^{3+}$:YLF Lasers near 2300 nm

**by**

**İsmail Yorulmaz**

**A Thesis Submitted to the**
**Graduate School of Sciences and Engineering**
**in Partial Fulfillment of the Requirements for**
**the Degree of**

**Doctor of Philosophy**
**in**
**Materials Science and Engineering**
**Koç University**

**December 2017**

Koç University

Graduate School of Sciences and Engineering

This is to certify that I have examined this copy of a doctor of philosophy thesis by

İsmail Yorulmaz

and have found that it is complete and satisfactory in all respects,
and that any and all revisions required by the final
examining committee have been made.

Committee Members:

_____

Alphan Sennaroğlu, Ph. D. (Advisor)

_____

Menderes Işkın, Ph. D.

_____

Uğur Ünal, Ph. D.

_____

Sarper Özharar, Ph. D.

_____

Gönül Eryürek, Ph.D

Date: _____

## ABSTRACT

Alexandrite ($Cr^{3+}$:$BeAl_2O_4$) and $Tm^{3+}$:YLF lasers are important, emerging solid-state lasers which generate coherent radiation in the near-infrared (700-820 nm) and mid-infrared (1800-2100 nm and 2200-2400 nm) regions of the electromagnetic spectrum, respectively. Both lasers have potential applications in diverse fields including biomedical imaging, surgery, ranging and spectroscopy.

The experimental studies presented in this thesis investigate both the continuous-wave diode pumping and pulsed operations of Alexandrite lasers near 760 nm and $Tm^{3+}$:YLF lasers near 2300 nm. In both cases, low threshold continuous-wave diode-pumped operation was demonstrated. In the case of the Alexandrite laser, pulsed operation was achieved by using the method of self-Q-switching. Passive Q-switching was employed in the case of the $Tm^{3+}$:YLF laser to generate pulses by using a $Cr^{2+}$:ZnSe saturable absorber.

The first part of the thesis focuses on the investigation of the temperature-dependent spectroscopic properties of the Alexandrite crystal and diode-pumped operation of the Alexandrite laser. First, the emission intensity and the fluorescence lifetime of Alexandrite were shown to decrease with increasing crystal temperature. Second, the diode-pumped laser performance was investigated in detail. In the laser experiments, the maximum output power of 48 mW was obtained with a slope efficiency of 36% at the input diode pump power of 170 mW. The laser slope efficiency decreased from 36% to 12% as the temperature of the gain medium was increased from room temperature to 200°C. Self Q-switching with pulse widths in the range of 5-15 μs and repetition rates in the range of 10-35 kHz was further observed by slightly changing the curved mirror separation of the cavity.

In the second part of this thesis, the continuous-wave operation of a 2.3-μm $Tm^{3+}$:YLF laser was investigated. First, the excitation spectrum of the $Tm^{3+}$:YLF was measured by using a tunable, narrow-linewidth $Ti^{3+}$:sapphire laser. Also, the average absorption cross-section of the 1.5 at. % $Tm^{3+}$:YLF was determined to be $0.77\times10^{-20}$ $cm^2$ by using power-

dependent and position-dependent absorption saturation data. A single-mode 120-mW diode laser was then used for pumping the $Tm^{3+}$:YLF laser cavity at 792 nm. In this configuration, low threshold lasing could be achieved with as low as 25 mW of input pump power by using a 1% output coupler. The maximum output power of 10.5 mW was obtained at 2305 nm with a slope efficiency of 11.4%. Second, by using a 250-mW diode laser, the threshold pump power and slope efficiency were measured as a function of effective output coupling. The minimum threshold pump power of 4 mW was measured at 0% output coupling. Power efficiency measurements showed that the highest slope efficiency of 10% was obtained around 0.7% output coupling and that the slope efficiencies beyond this output coupling decreased monotonically. The stimulated emission cross-section at 2305 nm was determined from the laser threshold data as $0.55\times10^{-20}$ $cm^2$.

The third part of this thesis focuses on the pulsed operation of the $Tm^{3+}$:YLF laser at 2.3 μm. To the best of our knowledge, passive Q-switching of a 2.3-μm $Tm^{3+}$:YLF laser was demonstrated for the first time by using a $Cr^{2+}$:ZnSe saturable absorber. The pulse durations and repetition frequencies of the passively Q-switched pulses were in the ranges of 1.2-1.4 μs and 0.3-2.1 kHz, respectively. By using the power-dependent repetition frequency data, the small-signal loss of the $Cr^{2+}$:ZnSe saturable absorber was further determined. In addition to passive Q-switching of the 2.3-μm $Tm^{3+}$:YLF laser, preliminary data on pulsing generated by using a semiconductor saturable absorber and a graphene saturable absorber are also presented. We foresee that both Alexandrite and 2.3-μm $Tm^{3+}$:YLF lasers operated in continuous-wave or pulsed regimes will find numerous scientific and technological applications.

## ÖZET

Alexandrite ($Cr^{3+}$:$BeAl_2O_4$) ve $Tm^{3+}$:YLF lazerleri elektromanyetik spektrumun yakın kızılaltı (700-820 nm) ve orta kızılaltı (1800-2100 nm ve 2200-2400 nm) bölgelerinde eş evreli ışıma yapan önemli, gelişen lazerlerdir. Her iki lazerin de biyomedikal görüntüleme, cerrahi, uzaklık tayini ve spektroskopi gibi çeşitli alanları içeren potansiyel uygulamaları vardır.

Bu tezde sunulan deneysel çalışmalarda, 760 nm civarında çalışan Alexandrite ve 2300 nm civarında çalışan $Tm^{3+}$:YLF lazerlerinin hem sürekli dalga diyotla uyarımı hem de darbeli olarak çalışmaları incelenmiştir. Her iki durumda da düşük eşik değerli sürekli dalga diyot pompalı çalışma rejimi gösterilmiştir. Alexandrite lazerinin darbeli olarak çalıştırılması, kendiliğinden Q-anahtarlama yöntemi kullanılarak elde edilmiştir. $Tm^{3+}$:YLF lazeri içinse, darbeler bir $Cr^{2+}$:ZnSe doyabilen soğurucu kullanılarak pasif Q-anahtarlama ile üretilmiştir.

Tezin birinci kısmında, Alexandrite kristalinin sıcaklığa bağlı spektroskopik özellikleri ile Alexandrite lazerinin diyot pompalı olarak çalıştırılması incelenmiştir. Öncelikle, Alexantrite kristalinin ışıma şiddeti ve floresans yaşam süresinin artan kristal sıcaklığına bağlı olarak azaldığı gösterilmiştir. Daha sonra, diyot pompalı lazer performansı ayrıntılı olarak incelenmiştir. Lazer deneylerinde, 170 mW pompa giriş gücü ile en yüksek 48 mW lazer gücü %36 verimle elde edilmiştir. Kazanç ortamının sıcaklığı, oda sıcaklığından 200 °C'ye çıkarıldığında ise, lazer verimi %36'dan %12'ye düşmüştür. Rezonatör çukur aynalarının konumu hafifçe değiştirildiğinde ise, 5-15 μs aralığında darbe genişlikleri ve 10-35 kHz aralığında darbe tekrar frekanslarına sahip kendiliğinden Q-anahtarlamalı darbeler gözlemlenmiştir.

Tezin ikinci kısmında, 2.3 μm $Tm^{3+}$:YLF lazerinin sürekli dalga çalıştırılışı incelenmiştir. Öncelikle, dar dalgaboyu genişliğine sahip $Ti^{3+}$:safir pompa lazeri kullanılarak $Tm^{3+}$:YLF kristalinin uyarım spektrumu ölçülmüştür. Ayrıca, $Tm^{3+}$:YLF kristalinin soğurma arakesiti, güce ve konuma bağlı soğurma doyumu verileri kullanılarak ortalama $0.77\times10^{-20}$ $cm^2$ olarak belirlenmiştir. Daha sonra 120mW güç veren tek kipli bir diyot lazer kullanılarak $Tm^{3+}$:YLF lazer rezonatörü 792 nm'de uyarılmıştır.

Bu konfigürasyonda %1 geçirgenliğe sahip çıkış aynası ve en düşük 25 mW pompa giriş gücüyle düşük eşik değerli lazer ışıması elde edilmiştir. Bu durumda, 2305 nm dalgaboyunda en yüksek 10.5 mW çıkış lazer gücü ve %11.4 güç verimi elde edilmiştir. Daha sonra, 250 mW çıkış gücü sağlayan bir diyot lazer kullanılarak eşik pompa güçleri ve güç verimleri çıkış aynası geçirgenliğinin bir fonksiyonu olarak ölçülmüştür. En düşük eşik pompa gücü %0 geçirgenliğe sahip çıkış aynası kullanıldığında 4 mW olarak ölçülmüştür. Güç verimi ölçümlerine göre en yüksek verim yaklaşık %0.7 çıkış geçirgenliğinde %10 olarak belirlenmiş ve daha yüksek geçirgenliklerde de verimin monotonik olarak azaldığı gözlemlenmiştir. Ayrıca, lazer eşik gücü ölçümlerinden 2305 nm dalgaboyundaki uyarılı ışıma arakesiti $0.55\times10^{-20}$ $cm^2$ olarak belirlenmiştir.

Tezin üçüncü kısmında, $Tm^{3+}$:YLF lazerinin, 2.3 μm dalgaboyunda darbeli olarak çalıştırılması üzerine odaklanılmıştır. Bildiğimiz kadarıyla, 2.3 μm $Tm^{3+}$:YLF lazerinin $Cr^{2+}$:ZnSe doyabilen soğurucu kullanılarak pasif Q-anahtarlamalı olarak çalıştırılması literatürde ilk kez gösterilmiştir. Pasif Q-anahtarlamalı darbelerin darbe süreleri ve darbe tekrar frekansları sırasıyla 1.2-1.4 μs ve 0.3-2.1 kHz aralıklarındadır. Güce bağlı darbe tekrar frekansı verisi kullanılarak $Cr^{2+}$:ZnSe doyabilen soğurucunun küçük sinyal kaybı belirlenmiştir. $Tm^{3+}$:YLF lazerinin pasif Q-anahtarlamalı çalıştırılmasına ek olarak, yarı iletken doyabilen soğurucu ve grafen doyabilen soğurucu kullanarak elde edilen ilk darbe verileri de sunulmuştur. Hem Alexandrite hem de 2.3 μm $Tm^{3+}$:YLF lazerinin sürekli dalga veya darbeli çalıştırılmalarının pek çok bilimsel ve teknolojik uygulamada yer alacağını öngörüyoruz.

## ACKNOWLEDGMENTS

Doctoral study is a long and challenging journey. Anyone who successfully manage to write a thesis, owe gratitude towards many.

First, I would like to thank my thesis advisor, Prof. Dr. Alphan Sennaroğlu for his immense help and invaluable suggestions during my Ph.D. study. In addition to his vast knowledge often consulted, his wisdom, guidance, and vision make him one of the best mentors that one could meet in a lifetime. I am grateful to him for providing me with this chance and allowing me to be a part of Laser Research Laboratory, at Koç University.

I would like to thank Menderes Işkın, Uğur Ünal, Sarper Özharar, and Gönül Özen Eryürek for taking part of my thesis committee. I am especially grateful to Uğur Ünal and Menderes Işkın for their valuable comments throughout the progress of my thesis for years.

I am indebted to Ümit Demirbaş, for the enthusiasm he shared with us. As an experimentalist, I learned a lot by having the opportunity to collaborate with him. I would like to thank Adnan Kurt for helping me in the technical difficulties of the experiments, inspiring me to 'make' things more professionally appealing. The things I learned from him helped me to tackle some of the problems I had encountered with electronics. I would also like to thank Ersen Beyatlı and Ferda Canbaz with whom I worked together in some of the projects in our group. They were always willing to help and open to fruitful discussions. I would like to thank M. Berk Bilgin and Ilyes Baali for their help in some of the experiments in this thesis.

I would like to thank some of the former and all current members of LRL: M. Natali Sözüdoğru, Ersen Beyatlı, Işınsu Baylam, Ferda Canbaz, Can Cihan, Abdullah Muti, Yağız Morova, Zehra İstemihan, and Gökhan Tanısalı for their support during my research.

I would like to thank Selçuk Çakmak, Muzaffer Bütün, and Muharrem Güler for sharing their expertise to overcome some of the technical difficulties of the electronics, optomechanics, and glassware.

I would like to thank Koç University not only for the financial support throughout my graduate studies, but also for providing excellent laboratories and lectures, and enthusiastic students at both undergraduate and graduate levels to create an intellectually stimulating atmosphere. I would like to thank TÜBİTAK for partially supporting this thesis through TÜBİTAK projects 114F185 and 113F199.

I would like to thank my friends M. Haroon Qureshi, Sultan S. Bukhari, Imran Khan, Abdullah Muti, Mustafa Eryürek. Abdullah Bilgin, Faruk Temur, Mustafa Yalçın, İsmail Ay, İsmail Yakin, Egemen Tuna, Yasin Karagöz for their support. They presented to me good advice, pleasant time, delicious food (especially Indo-Pak cuisine), and, prayers and loans even without asked for them.

I am thankful to my wife Esra, for her understanding, patience, devotion and unconditional love. I would like to thank my parents, parents-in-law, and brothers for their love and support. I owe too much to my father Abdullah Yorulmaz, to my father-in-law Prof. Dr. Bayram Dalkılıç and my brothers Yunus Emre and Dr. Mustafa Yorulmaz for their encouragement and guidance throughout my education.

*I dedicate this thesis to my mother Ayşe Yorulmaz and father Abdullah Yorulmaz.*

## TABLE OF CONTENTS

## LIST OF FIGURES

## NOMENCLATURE

| | |
|---|---|
| $\alpha_{p0}$: | small-signal differential absorption coefficient |
| A: | area / absorption |
| $A_{eff.}$: | effective area |
| $A_{g.}$: | ground state absorption |
| c: | speed of light in vacuum |
| d: | distance |
| E: | electric field |
| $E_p$: | photon energy / pulse energy |
| f: | focal length |
| $f_p$: | focal length |
| $f_{rep:}$ | repetition rate of the pulses |
| $G_{0:}$ | small-signal gain |
| h: | Planck's constant |
| $I_L$: | laser intensity |
| $I_p$: | pump intensity |
| $I_{sat}$: | saturation intensity |
| J: | total angular momentum number |
| $J_{sat}$: | saturation fluence |
| k: | Boltzman constant |
| L: | total loss of the resonator / total orbital angular momentum number |
| $l_m$: | length of the gain medium |
| M: | M-square parameter / mirror |
| n: | refractive index |
| $n_2$: | nonlinear refractive index |
| $N_T$: | Total ion density |
| $\eta$: | slope efficiency |
| $\eta_a$: | small-signal pump absorption |
| $\eta_p$: | efficiency of pumping |
| $\theta_i$: | incident angle |
| $\theta_B$: | Brewster angle |

$\lambda_L$: laser wavelength

$\lambda_p$: pump wavelength

$\nu_L$ laser frequency

$\nu_p$: pump frequency

q: q-paramater of the beam

P: power

$P_{cr}$: critical power

$Q_0$: small-signal loss

R: reflectivity

S: spin quantum number

σ: Pauli matrices / optical conductivity

$\sigma_a$: absorption cross section

$\sigma_e$: stimulated emission cross section

$\tau_f$: fluorescence lifetime

T: transmission / temperature

w: spotsize

$w_0$: beam waist

# Chapter 1: Introduction

## 1.1 Lasers: A brief overview

In the last nearly six decades, following the first demonstration of lasing at optical frequencies, lasers have attracted a great deal of attention and found a diverse spectrum of applications in science and technology. The richness of these applications stems from the unique properties of lasers that are unequalled by any other conventional light source. Lasers produce monochromatic, coherent, spectrally bright and directional light waves and these properties distinguish them from other light sources. The unique properties of laser emission are directly related to how lasing is achieved. First and foremost, the laser is an oscillator and combines optical amplification with positive feedback provided by an optical resonator. For example, the directionality of the laser output results from the use of a one-dimensional resonator. As such, the boundary conditions imposed by the resonator architecture lead to the generation of an intense light beam directed along the optical axis of the resonator.

The mechanism of optical amplification is based on stimulated emission which leads to the emission of photons with identical wavelength and phase. Stimulated emission was first predicted by Albert Einstein in his seminal paper published in 1917 [1], where he described a two-level atomic system and explained the elementary quantum processes of radiation: absorption, spontaneous emission and stimulated emission. In this model, a photon is absorbed only when its energy matches the difference between the upper and lower energy levels of the atomic system. The light emission is, however, either spontaneous in time or it happens when a resonant photon interacts with the excited atomic system to induce a downward transition. A downward transition of this kind results in the emission of photons with identical wavelength and phase. Also, the emitted

photons propagate in the same direction as the stimulating photons passing through the gain medium.

The first device which uses the stimulated emission phenomenon was invented by Charles H. Townes, James P. Gordon, and H. J. Zeiger in 1953 [2]. They used a microwave cavity and ammonia molecules as the gain medium inside the cavity. In 1960, Theodore Maiman invented the first laser oscillator operating at optical frequencies. This consisted of a flash-lamp pumped ruby crystal [3]. Upon increasing the pumping energy, sufficient population inversion was achieved and the emission at 694.3 nm wavelength was narrowed as an indication of stimulated emission. Following the first demonstration of the ruby laser, several different kinds of the lasers quickly emerged. Maiman's first laser was followed by the gas laser [4], fiber lasers [5], semiconductor lasers [6] and liquid dye lasers [7] within a few years. In addition to these more conventional laser types, more exotic laser systems based on optical microcavities [8], biological substances such as human blood [9], and even living cells were demonstrated [10]. Each laser type has different properties which make it suitable for a particular application.

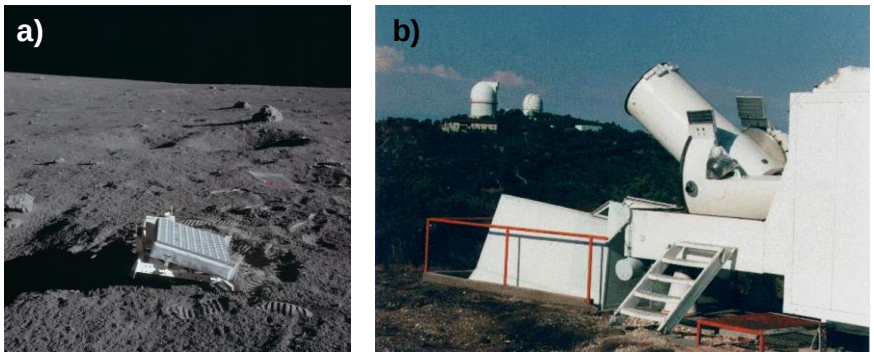


*Fig. 1.1 a) Array of retroreflectors deployed by the astronauts during Apollo 14 mission for the accurate measurement of the distance between the Moon and the Earth (Courtesy of Apollo Lunar Surface Journal, NASA) [11]. b) McDonald Laser Ranging Station at University of Texas, USA [12].*

One of the first interesting applications employing the unique properties of lasers was the accurate measurement of the Moon's distance from the Earth in 1962 [13]. Following these first experiments employing lasers, in 1971, an array of retroreflectors was deployed

on the moon as part of the Apollo 14 Mission to enhance the accuracy (Fig. 1.1 a)). The earth to moon distance was measured with a Q-switched ruby laser directed to the retroreflector array on the moon coupled to a telescope in the McDonald Laser Ranging Station in Texas, USA (Fig 1.1 b)) [14]. Since then, lasers were used in numerous applications such as ranging [15], medical imaging [16], precision cutting [17] or welding [18], additive manufacturing [19], directed-energy weapons [20], and precision clocks [21]. The use of lasers also triggered other scientific breakthroughs. For instance, the first demonstration of the second harmonic generation [22] and the production of early holograms [23, 24] owe much to the invention of lasers and their unique properties. Moreover, numerous scientists received the Nobel Prize for their breakthrough achievements in the field of lasers: These include Townes, Basov and Prokhorov for their studies which led to the invention of lasers (1964); Gabor for the invention and development of holography (1971); Bloembergen and Schawlow for laser spectroscopy (1981); Chu, Cohen-Tannaudji, and Philips for optical trapping and cooling of atoms with laser light (1997); Zewail for femtosecond spectroscopy (1999); Hall and Hänsch for frequency comb technique (2005), and Betzig, Hell, and Moerner for super-resolved fluorescence microscopy (2014) [25, 26].

Also, ultrashort optical pulse generation is another important scientific field made possible by use of lasers. The generation of such pulses are particularly important for applications requiring ultrashort time resolution or high peak powers that can be obtained from ultrafast lasers. For example, the isomerization of the rhodopsin molecule in the retina was determined at the femtosecond timescale to explain the vision process [27].

Although invented decades ago, the numerous application fields of lasers generated a never-ending interest in the field of developing novel laser sources. In this thesis, we developed diode-pumped Alexandrite and 2.3-μm $Tm^{3+}$:YLF lasers and demonstrated their low threshold, continuous-wave and pulsed operations [28, 29]. In the following subsections of this chapter, we will give a brief introduction to the spectroscopic properties of transition metal and rare-earth doped solid-state lasers, provide literature

review of Alexandrite and 2.3-μm $Tm^{3+}$- doped lasers and finally state the original contributions of this thesis work.

In Chapter 2, the experimental results obtained with a diode-pumped, low threshold Alexandrite laser will be provided. In Chapter 3, continuous-wave $Tm^{3+}$:YLF laser results will be explained in addition to the excitation spectrum and saturation behavior of the $Tm^{3+}$:YLF laser. In Chapter 4, passively Q-switched operation of the 2.3 μm $Tm^{3+}$:YLF laser will be described. In Chapter 5, preliminary experimental results obtained with a for graphene mode-locked $Tm^{3+}$:YLF laser at 2.3 μm will be presented. The conclusions of the thesis will be provided in Chapter 6.

## 1.2 Spectroscopic properties of transition metal and rare-earth doped solid-state lasers

Solid-state laser gain media are crystalline, ceramic or glass hosts doped with laser-active ions. Solid-state hosts are better host materials for the laser-active ions because they do not quickly degrade compared to the gas and liquid gain media. When doped with a few atomic percent of a laser-active ion, they can potentially work as robust gain media for a long period without any chemical degradation. Both the crystallography of the laser host material, and the spectroscopy of the appropriate laser-active ion are important areas of study. This part aims at summarizing the fundamental aspects of the laser active ions $Tm^{3+}$ and $Cr^{3+}$ since they are directly related to the current thesis work. In particular, these two ions appear inside the $Tm^{3+}$:YLF and Alexandrite ($Cr^{3+}$:$BeAl_2O_4$) crystals which were employed as gain media in the experiments.

In the previous section, we mentioned that radiative emission takes place in downward transitions from the energy levels of an atomic system. The electronic configurations of the elements or ions can be determined by using quantum mechanical tools. In particular, Hund's rules can be used to determine the ground-state spectroscopic designation. Selection rules are further employed to determine which transitions are allowed.

We next discuss how the ground-state configuration of the $Tm^{3+}$ ion is determined. Trivalent rare-earths have $4f^n$ electronic configuration. Their electron configurations are

expressed as $RE^{3+}$:[Xe] $4f^n$. Here, [Xe] stands for the electron configuration of the inert xenon atom:

$$[Xe]: 1s^2\ 2s^2\ 2p^6\ 3s^2\ 3p^6\ 3d^{10}\ 4s^2\ 4p^6\ 3d^{10}\ 5s^2\ 5p^6.$$

Primarily, $4f^n$ orbital is electrostatically shielded by $5s^2$ and $5p^6$ shells of the xenon atom. This shielding reduces the effect of even the nearest neighbors in the crystal field, and energy level positions are not greatly influenced by the host. Hence, the emission lines do not vary significantly from host to host.

Since a major part of this thesis was dedicated to $Tm^{3+}$:YLF lasers, the determination of the ground state of the $Tm^{3+}$ ion is shown below as an example. The energy levels were named by the standard atomic term designation, $^{(2S+1)}L_J$. Here, S is the spin quantum number, L is the total orbital angular momentum number, and J is the total angular momentum number ((L+S) or (L-S) for the shell which is more than half full or less than half full, respectively). L can take integer values of 0, 1, 2, 3, 4, 5, 6 and represented by the term symbols S, P, D, F, G, H, and I. As an example, $Tm^{3+}$ ion consists of 66 electrons and it has the following electron configuration: $Tm^{3+}(66)$: $[Xe]4f^{12}$. In the last shell, there are 12 electrons. F orbitals have orbital quantum numbers l = 0, 1, 2, 3 and hence magnetic quantum numbers, $m_l$ = +3, +2, +1, 0, -1, -2, -3. We fill in the electrons according to the Aufbau principle, which states that the electrons should be placed in atomic orbitals giving the lowest energy configuration as shown below:

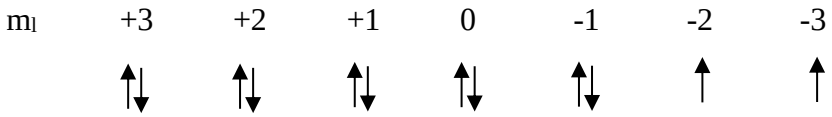


There are two unpaired electrons, S = 2×½ = 1. The resultant total orbital quantum number is the sum of $m_l$ values: L = (2×3) + (2×2) + (2×1) + (2×-1) + (-2) + (-3) = 5. This corresponds to the H-state. The highest value of J is the sum of Land S, J = L+S=5+1=6. The ground state atomic term designation of $Tm^{3+}$ is therefore $^3H_6$.

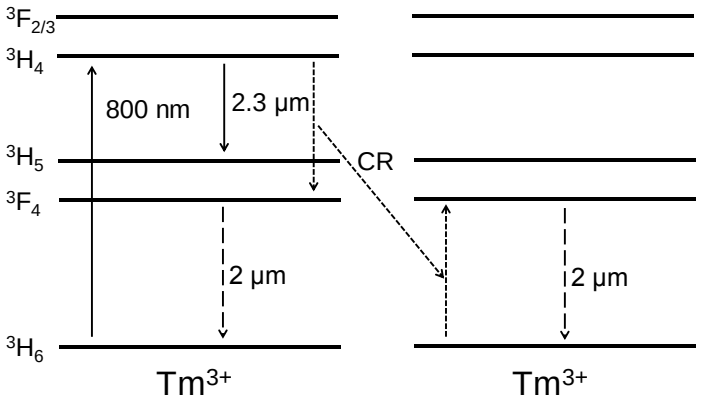


*Fig. 1.2 Energy level diagram of $Tm^{3+}$ ions involving 2.3 µm and 2 µm laser transitions.*

The energy level diagram of the $Tm^{3+}$ ion involving 2.3-µm and 2-µm laser transitions is given in Fig.1.2. For both laser wavelengths, 800 nm pumping can be utilized for transition to the upper $^3H_4$ level. The 2.3-µm laser transition of $Tm^{3+}$ ion takes place directly between $^3H_4$ and $^3H_5$ levels. However, for 2-µm emission, a nonradiative depopulation to $^3F_4$ level is followed by $^3F_4 \rightarrow {}^3H_6$ transition. Another mechanism important for both wavelengths is cross relaxation. In cross-relaxation, an excited $Tm^{3+}$ ion makes a nonradiative transition by exciting another nearby ion to the $^3F_4$ level, resulting in two ions at the same level. The cross-relaxation mechanism is a concentration dependent phenomenon which allows the non-radiative transfer of energy from one ion to another and hence generates two laser photons for each pump photon. Although cross relaxation ideally doubles the quantum efficiency of the 2-µm emission, it nonradiatively depletes the $^3H_4$ laser level of the 2.3-µm transition. For this reason, for 2.3-µm-thulium lasers, the concentration of $Tm^{3+}$ ions is kept below 2% [30]. The second important physical phenomenon for the 2.3-µm transition of the $Tm^{3+}$ ion is the role of phonon interaction. The host material should have low multiphonon relaxation rates, which then leads to longer upper-state lifetimes. Fluoride hosts are suitable because of their low phonon energies (YLF crystal = 560 $cm^{-1}$ [31]). Hence, a 1.5 at. % doped $Tm^{3+}$:YLF crystal was used in the 2.3-µm laser experiments.

Another group of laser active ions in the Periodic Table includes transition metal ions such as, $Co^{2+}$, $Fe^{2+}$, $Cr^{3+}$, $Ti^{3+}$, and others. The 3d orbitals are larger in size compared to the 4f electrons. Hence, they are prone to the effects of the crystal field of the host, unlike 4f ions which have a shielding by the larger $5s^2$ and $5p^6$ orbitals. For this reason, they are affected by the crystal field, resulting in different spectroscopic properties depending on the host material used. For example, $Cr^{3+}$ have $3d^5$ electron configuration. d orbitals are five-fold degenerate when there is no external field applied. However, in an octahedral field, for example, where active ions are at the center of a cube of identical neighboring ions, 5d orbitals are split into one triply- degenerate and one doubly-degenerate orbital. Consequently, there are two kinds of transitions: the first kind involving the change of the spin in the same energy level (spin-flip) and the other resulting from band transition.

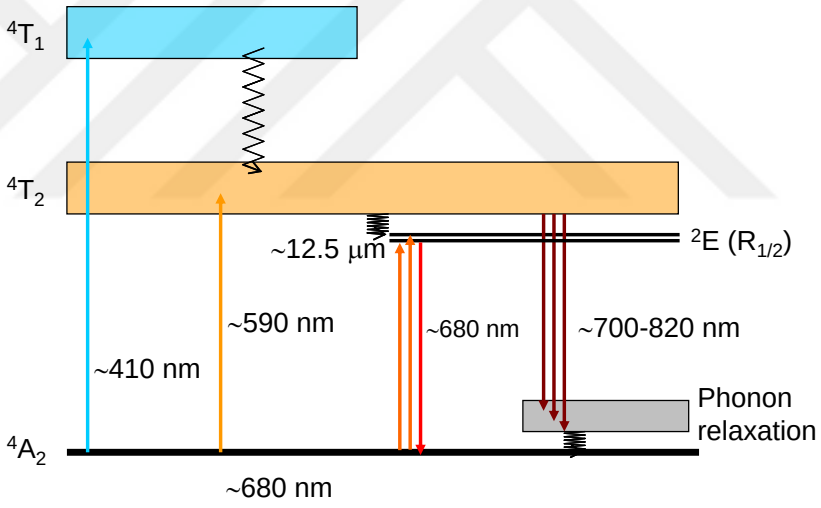


*Fig. 1.3 Energy levels of Alexandrite.*

The energy level diagram of the $Cr^{3+}$ ions in the Alexandrite crystal is given in Fig 1.3. Alexandrite has two broad absorption bands in blue (410nm, $^4A_2 \rightarrow {}^4T_2$ transition) and green (590nm, $^4A_2 \rightarrow {}^4T_1$ transition) [32, 33]. In addition to these, there are also two narrow absorption peaks, one at 680.4 nm and the other at 678.5 nm namely, R1 and R2 transition lines. The lifetime of the $^2E$ state is too long (1.54 ms) compared to the lifetime of the $^4T_2$ (6.6 µs) and, therefore, it behaves as an energy storage for the $^4T_2$ level. The

$^4T_2$ and $^2E$ level are separated only 800 $cm^{-1}$ (a few kT at room temperature, where k is Boltzmann's constant and T is about 300 K) and thus, for most of the cases $^4T_2$ level is also populated by phonon interactions. Although the ruby laser has a similar energy level diagram with the same ($Cr^{3+}$) active ion, due to the difference in the host materials the level difference between $^4T_2$ and $^2E$ is 2300 $cm^{-1}$ and therefore it is not tunable as Alexandrite. This difference demonstrates to what extent the host material affects the emission properties of transition metal ions.

## 1.3 Previous studies conducted with Alexandrite lasers and 2.3-µm $Tm^{3+}$-doped lasers

### 1.3.1 Alexandrite lasers

Alexandrite (chromium-doped chrysoberyl, $Cr^{3+}$:$BeAl_2O_4$) is one of the earliest solid-state lasers invented in early 1970's [34, 35]. It was the first tunable solid-state laser [35], and also the first directly diode-pumped tunable solid-state laser at room temperature [36]. It was the third $Cr^{3+}$-doped laser crystal after ruby [3] and $Cr^{3+}$:YAG [37]. Alexandrite has many superior properties as a laser crystal, and therefore is still used in many modern laser architectures. The main assets of Alexandrite laser are mainly based on its broad tunability and superior thermal and mechanical properties. Alexandrite is five times more durable to fracture and has two times greater thermal conductivity when compared to $Nd^{3+}$:YAG which is one of the most widely used laser crystals in industrial lasers [38]. In addition to industry, $Nd^{3+}$:YAG lasers were used in space and military for a long time, where the special standards limit the variety of the lasers that can be used [39]. The superior physical properties make Alexandrite an alternative gain media for space-borne differential absorption lidar (DIAL) applications where tunability and tuning range is particularly important [40]. Although $Nd^{3+}$:YAG lasers have long heritage in space applications, it has only a single, narrow laser line at 1064 nm. Higher harmonics (532 nm, 355nm and, 266 nm) with optical parametric methods can be produced at discrete wavelengths which evidently increases the cost and complexity of the laser system. Alexandrite, however, is broadly tunable in addition to its excellent thermal and

mechanical properties, allowing to operate the laser even in Antarctic polar conditions [41]. It also allows maintenance-free temperature tuning of the laser wavelength.

For further investigation, we can compare Alexandrite laser with $Ti^{3+}$:sapphire, both of which are broadly tunable solid-state lasers. Alexandrite has higher $\sigma_e \tau_f$ (emission cross section × fluorescence lifetime of the laser level) values than $Ti^{3+}$:sapphire, product of which is inversely proportional to the achievable threshold pump power. Therefore, higher $\sigma_e \tau_f$ product of Alexandrite, in principle, allows operation with lower threshold pump powers [42]. Moreover, having strong absorption lines in the red region allows pumping with well-developed red diode lasers (AlGaInP operating in the 630 nm-680 nm range) in low-cost and efficient pumping geometries. For the 760-nm laser wavelength, red diode pumping allows operation with higher quantum efficiency. In the case of $Ti^{3+}$:sapphire laser however, the gain medium does not have an absorption line in the red region and to date, it has been generally pumped with more costly green lasers [43].

The first Alexandrite lasers were pumped with flash-lamp [44-48] and arc-lamp [49, 50], and operated at 760 nm with moderate energy levels. Diode lasers were later used for pumping Alexandrite, after the emergence of diode lasers emitting in the red [36, 51-55]. Also, by using a single emitter providing 170 mW of output power, low threshold operation of the Alexandrite laser was demonstrated [29]. The maximum output power of 26 W was obtained by pumping Alexandrite lasers with high-power laser diodes [56]. Recently, high power LEDs (light emitting diodes) were also used to pump Alexandrite lasers generating 3-mJ energy at 748 nm [57]. A wavelength tunable diode-pumped Alexandrite laser was passively Q-switched by utilizing a SESAM and produced 550-ns pulses [58]. Pulsed operation of Alexandrite in the femtosecond regime was realized in regenerative amplifiers [59]. Kerr-lens mode-locked Alexandrite laser with 170-fs pulses was also demonstrated by using a 7-W green pump laser [60].

### 1.3.2 2.3-μm $Tm^{3+}$-doped lasers

Laser emission of $Tm^{3+}$-doped media has been demonstrated at various wavelengths. The laser emission at 2.3 μm based on the $^3H_4 \rightarrow {}^3H_5$ transition [61], from 1.8 μm to 2.1

μm based on the $^3F_4 \rightarrow {}^3H_6$ transition [62], and in the near-infrared (NIR) region at 0.8 μm based on the $^3H_4 \rightarrow {}^3H_6$ transition (cryogenic temperatures) [63] was demonstrated, among others. The laser sources based on $Tm^{3+}$-doped gain media have been used in medicine, remote sensing, and as pump sources for reaching longer/shorter wavelengths by high harmonic generation and for optical data storage. Particularly, 2.2-2.4-μm wavelength range laser sources have many practical uses in remote sensing, medicine and photonics. Many of the atmospheric pollutants such as CO, HF, $H_2CO$ and $CH_4$ have strong absorption in this range [64-66]. Especially, 2.3-μm wavelength is the first water absorption free window for CO detection [67] and lasers operating in this range can be used for noninvasive blood glucose measurements [68, 69]. Another important use of mid-IR lasers is in pumping optical parametric oscillators (OPOs) to reach higher wavelengths. For example, many OPOs consisting of ZGP crystals are pumped with $Tm^{3+}$:$Ho^{3+}$ co-doped [70] or $Tm^{3+}$-pumped Holmium lasers [71]. Using the 2.3-μm laser line of the $Tm^{3+}$-doped gain media instead, will be more advantageous for two reasons. First, the ZGP crystal has smaller absorption coefficient at 2.3 μm and absorption-induced heating effects will be minimized. Second, 2.3-μm laser radiation can be readily generated by using low-cost diode lasers around 800 nm, as discussed in Chapter 3.

2.3-μm laser emission based on $Tm^{3+}$-doped gain media was first demonstrated in early 1970's following the predictions based on the Judd-Ofelt theory. The first examples of these lasers utilized $Cr^{3+}$ co-doped oxides with flash-lamp pumping. Later, the continuous-wave operation of the laser was demonstrated by Pinto et al. between 2.2 μm to 2.46 μm using $Tm^{3+}$:YLF gain medium [61]. Other than bulk crystals, 2.3 μm-laser emission of $Tm^{3+}$-ion was further shown in fibers in both continuous-wave (cw) and gain-switched operation regimes. The optimum concentration of the $Tm^{3+}$-doped gain media was further determined as 1.5 at. %, based on the spectroscopic experiments carried out to reduce the unwanted nonradiative decay processes [30]. Furthermore, the high-power cw operation of $Yb^{3+}$:$Tm^{3+}$:YLF laser was reported by using 685-nm and 960-nm pump diodes [72]. Recently, pulsed operations of the 2.3-μm $Tm^{3+}$:YLF laser were also reported in passive Q switching regime with a $Cr^{2+}$:ZnSe saturable absorber [28], passive

mode locking regime with a semiconductor saturable absorber mirror (SESAM) [73], and Kerr-lens mode-locking regime [74].

### 1.4 Contributions of the thesis work

The contributions of this thesis on Alexandrite lasers mainly focus on low-threshold and efficient diode-pumping schemes [29]. The described geometry allowed the operation of the Alexandrite laser with as low as 13 mW of pump power. We demonstrated 36% power slope efficiency and generated a maximum output power of 48 mW with 0.5% output coupler, by using a single-mode diode laser providing up to 170 mW at 635 nm. The laser was tunable from 736 nm to 795 nm at room temperature. Furthermore, the laser was tuned from 776 nm to 823 nm by increasing the crystal temperature to 200 ºC. The temperature dependent laser performance results indicated that slope efficiency and output power decreased with increasing temperature. Roundtrip cavity losses were estimated to be 0.25 %. Self Q-switched operation was obtained with slight misalignment of the laser resonator. In this regime, pulse durations were between 5 and 15 μs and pulse repetition frequencies were in the 10-35 kHz range. Furthermore, spectroscopic properties at elevated temperatures up to 300 ºC were measured. The lifetime of the of the Alexandrite crystal decreased with increasing temperature. As a result, we provided important and useful experimental data that summarize the low-threshold diode-pumped performance of the laser, as well as temperature-dependent characteristics of the emission spectrum and laser power efficiency.

The parts of this thesis involving the 2.3-μm $Tm^{3+}$:YLF laser consist of continuous-wave and Q-switched laser results. In the continuous-wave study, we determined the best pumping band near 800 nm by measuring the excitation spectrum. By analyzing the absorption saturation data, the absorption cross section was experimentally determined and was found to be close to the literature values In addition to the $Ti^{3+}$:sapphire-pumped experimental continuous-wave laser results, two different diode lasers were also used to pump the $Tm^{3+}$:YLF crystal. 2.3-μm laser emission from $Tm^{3+}$:YLF was obtained with a single-emitter providing 120 mW of output power. The laser threshold pump power was

25 mW when a 1% output coupler was used. 10.5 mW of output power at 2305 nm was obtained with 11.4% slope efficiency

The pulsed operation of the 2.3-μm $Tm^{3+}$:YLF laser was also investigated. The first pulsed laser results from a 2.3-μm $Tm^{3+}$-doped gain medium was demonstrated [28]. Passive Q-switching behavior was obtained by using a $Cr^{2+}$:ZnSe saturable absorber in the laser cavity. The repetition rate and the pulse duration of the Q-switched pulses were in the range 1.2 μs-1.4 μs and 0.3-2.1 kHz range, respectively.

In addition to passive Q-switching results, preliminary results of mode locking based on graphene saturable absorber was also demonstrated. In this part, a mode-locked spectrum with a FWHM (full width at half maximum) bandwidth of 1.9 nm (indicating picosecond-long pulses when a $sech^2$ pulse profile is assumed) was obtained. The radio-frequency (RF) peak had a contrast of more than 57 dB with respect to the noise floor at the fundamental frequency of the mode-locked pulse train (103.9 MHz). By careful dispersion compensation, we expect that it should be possible to obtain significantly shorter femtosecond pulses from the 2.3-μm $Tm^{3+}$:YLF laser based on graphene mode locking.

# Chapter 2

## Diode-pumped and low-threshold Alexandrite laser

In this chapter, we will describe the experimental results of continuous-wave and self-Q-switched operation of a diode-pumped, low-threshold, and continuous-wave Alexandrite laser. Temperature-dependent lifetime data of two different Alexandrite crystals will be presented. Also, the measured emission spectra of the Alexandrite crystal used in laser experiments were examined for crystal temperatures up to 300 °C. In the laser experiments, the continuous-wave laser power efficiencies, threshold pump powers, tuning ranges will be reported. Furthermore, the temperature dependent laser performance will be explained using the measured laser slope efficiencies and wavelength tuning for elevated temperatures up to 200 °C. Lastly, we will describe the experimental results of self-Q-switching in Alexandrite laser.

### 2.1 Experimental setup

In our experiments involving the temperature-dependent spectroscopy of Alexandrite, we used two different Brewster/Brewster cut crystals. The crystals were doped with 0.13 at. % $Cr^{3+}$ and 0.2 at. % $Cr^{3+}$ ions and having length×width×thickness dimensions of 8 mm×5 mm×3 mm and 8 mm×5 mm×3 mm, respectively. Both crystals were Brewster-cut for minimizing the Fresnel loss and polished in E//b orientation to achieve maximum absorption of the pump wavelength. The crystals were mounted on a copper crystal holder and surrounded with gold foil to facilitate heat conduction. The temperature of the crystals was determined by adjusting the temperature of the crystal holder in the 25 - 300 °C range.

Frequency-doubled output of a commercial $Nd^{3+}$:$YVO_4$ laser at 532 nm with full-width-half-maximum pulse widths of around 70 ns and a repetition frequency of 250 Hz was used in emission spectrum and lifetime measurements. The measurements were

carried out with pulse energies of about 1 μJ. For both measurements, the pump beam was focused nearly at the center of the crystal with a beam waist of nearly 25 μm using a convex lens with a focal length of 6 cm. The emission signal was collected with a $MgF_2$ focusing lens (f=8 cm). A commercial CCD spectrometer with a resolution of 1.5 nm and a spectral responsivity in the region between 200 nm and 1100 nm was used for the emission spectrum measurements (USB2000, Ocean Optics, Inc.). For the lifetime measurements, a 1-GHz silicon photodetector detector and a 500-MHz digital sampling oscilloscope were used. The emission spectrum and the fluorescence lifetime were measured for the temperatures ranging from 25 °C to 300 °C. We note here that the calculated temperature difference between the copper edge and the center of the crystal is at most 2-3 °C due to the relatively high thermal conductivity of the laser crystal. Hence, we assume that the measured temperature of the crystal holder is nearly the same as the temperature of the laser crystal at the position of the beam.

Figure 2.1 shows the experimental setup of the diode-pumped, continuous-wave (cw) Alexandrite laser. A single-mode, 635-nm laser diode (AlGaInP) was used as the pump source. The temperature of the single-mode diode (SMD) was kept at 20 °C with a thermoelectric cooler. The laser diode had a maximum output power of 170 mW at the driving current of 300 mA. The output of the laser diode was collimated by a plano-concave lens with a focal length of 4.5 mm. An anti-reflection (AR) coated 2× anamorphic prism pair was used to obtain a circular beam from the elliptical output of the SMD. The output of the SMD was then focused inside the Alexandrite crystal using an AR- coated focusing lens (L2, $f_2$=60 mm). An astigmatically compensated, 4-mirror x-cavity was built by using two curved high reflectors (CM1 and CM2, each with a radius of curvature of 75 mm), a flat high reflector (HR), and an output coupler mirror. The coating of the cavity high reflectors was designed to reflect more than 99.9 % from 750 nm to 850 nm. The pump mirror (CM1) was AR-coated for minimizing the reflection losses to transmit more than 95% of the bump beam around 650 nm. The laser cavity had a 55-cm HR arm and 30-cm OC arm, which supports an estimated laser beam waist of around 25 μm near the center of the Alexandrite crystal. By using the described laser

cavity, the continuous-wave laser power performance for different crystal temperatures and output couplers with different transmissions was investigated. For continuous-wave laser tuning experiments, a quartz birefringent tuning plate was used in the HR arm.

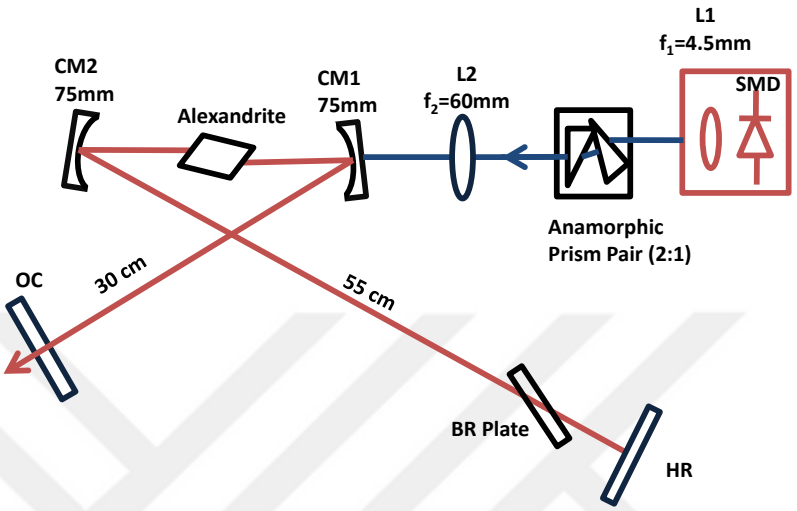


*Fig. 2.1 Schematic of the cw Alexandrite laser pumped with a single-mode diode laser. SMD: Single-mode diode, BR plate: Birefringent plate for laser wavelength tuning, OC: Output coupler.*

## 2.2 Temperature-dependent emission and lifetime spectroscopy of Alexandrite

The energy level diagram of the Alexandrite crystal (Fig. 1.3) was described earlier in Section 1.2. Regarding the energy level diagram, we stated before that $^2E$ acts as a storage level for the $^4T_2$ level and the $^4T_2$ level is partially populated due to the small energy difference between these levels. Also, the four-level laser operation of the Alexandrite laser is due to the transition from the $^4T_2$ level to the $^4A_2$ level. Therefore, the temperature dependence of the emission spectrum and fluorescence decay time for the $^4T_2$ and $^2E$ levels were investigated to provide a deeper insight into the laser parameters at elevated temperatures.

Figure 2.2 shows the measured fluorescence lifetime variation as a function of the crystal temperature in the 25 °C - 300 °C range. For these measurements, Alexandrite crystals with $Cr^{3+}$ doping levels of 0.13 % and 0.2 % were used. The measured lifetimes at all temperatures were in good agreement with different crystal samples, indicating that the dynamics of fluorescence does not change considerably for the 0.13 % and 0.2 % $Cr^{3+}$

concentration levels. The previous studies also reported that Alexandrite does not have the concentration quenching effect [75]. At 25 °C crystal temperature, fluorescence lifetimes of the Alexandrite crystals were measured as 262 µs and 268 µs for the 0.13% and 0.2% $Cr^{3+}$-doped samples, respectively. The experimental error of this measurement was on the order of ±5 µs. Therefore, they can be considered as the same. Also, the lifetime measurement is in good agreement with the previously reported results (262 µs in [76]).

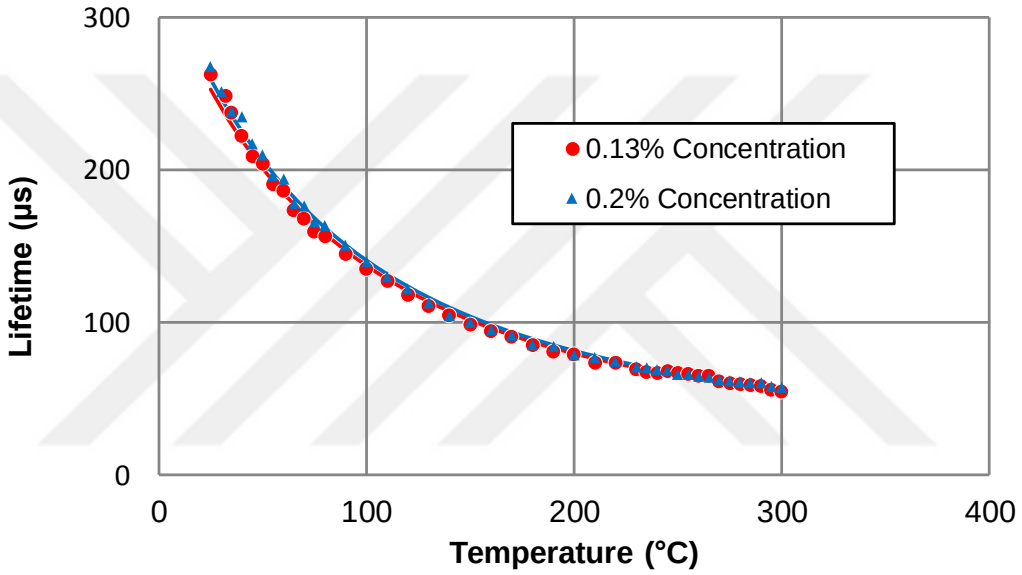


*Fig. 2.2 Measured variation of the fluorescence lifetime as a function of the crystal temperature for the Alexandrite crystals doped with 0.13 % and 0.2 % $Cr^{3+}$-concentration.*

As the temperature increases, the measured lifetime decreases monotonically and reaches a value of 55 µs at 300 °C for both samples. A similar decrease in the lifetime was reported in the literature for this temperature range [76].

The temperature dependence of the fluorescence lifetime ($\tau_F(T)$) could be modeled by using the Mott equation for the transition metal ion-doped laser materials [77, 78]:

$$\frac{1}{\tau_F(T)} = \frac{1}{\tau_R} + \frac{1}{\tau_{NR}(T)} = \frac{1}{\tau_R} + \frac{1}{\tau_{NR\,0}} \mathrm{Exp}\left(-\frac{\Delta E}{kT}\right). \quad (2.1)$$

Here, $\tau_R^{-1}$ is the spontaneous radiative decay rate, $\tau_{NR}(T)^{-1}$ is the temperature-dependent non-radiative decay rate, $\tau_{NR0}^{-1}$ is the high-temperature limit of the non-radiative decay rate, $\Delta E$ is the activation energy, k is the Boltzmann's constant and T is the absolute temperature, in Kelvin. As can be seen from this equation, the fluorescence lifetime decreases with increasing temperature due to the increase in the rate of phonon interactions. The solid lines in Fig. 2.2 shows the least-squares fit to the lifetime data. Here, the low-temperature value of the fluorescence lifetime of the Alexandrite ($\tau_R$=1540 μs) was used, asreported before in the literature [76]. The best-fit values for $\tau_{NR0}$ and $\Delta E$ were determined to be 9.51 μs and 717 $cm^{-1}$, and 9.55 μs and 722 $cm^{-1}$, for the 0.13 % and 0.20 % chromium-doped Alexandrite crystals, respectively. These values are in good agreement with the values of $\tau_{NR0}$ and $\Delta E$ (6.6 μs and 800 $cm^{-1}$ [76]) reported in the previous studies. We note here that, for the temperatures up to around 70 K (-200 °C), the fluorescence lifetime of the $^4T_2$ level was reported to be increasing with temperature [76]. This is due to a thermal excitation of ions in the $^2E$ level which is actually a doublet, and the upper lying level has a longer lifetime [76]. The $^4T_2$ laser level, has a lifetime of around 10 μs, and therefore the transition to this level reduces the overall fluorescence lifetime. At elevated temperatures, the excited ions in the reservoir level ($^2E$) are transferred to the $^4T_2$ laser level, due to the interaction of these levels through phonons. As a result, at elevated temperatures, the phonon interactions increase and hence reduces the effective fluorescence lifetime of the system. Besides, this interaction enhances the effective stimulated emission cross section of the $^4T_2$ level [79]. Therefore, despite the observed decrease in the fluorescence lifetime, using a pulsed pump source with pulse durations shorter than the fluorescence lifetime, the laser efficiency was shown to improve by increasing the crystal temperature. This way, the increase observed in stimulated emission cross section enhances the overall laser efficiency [80].

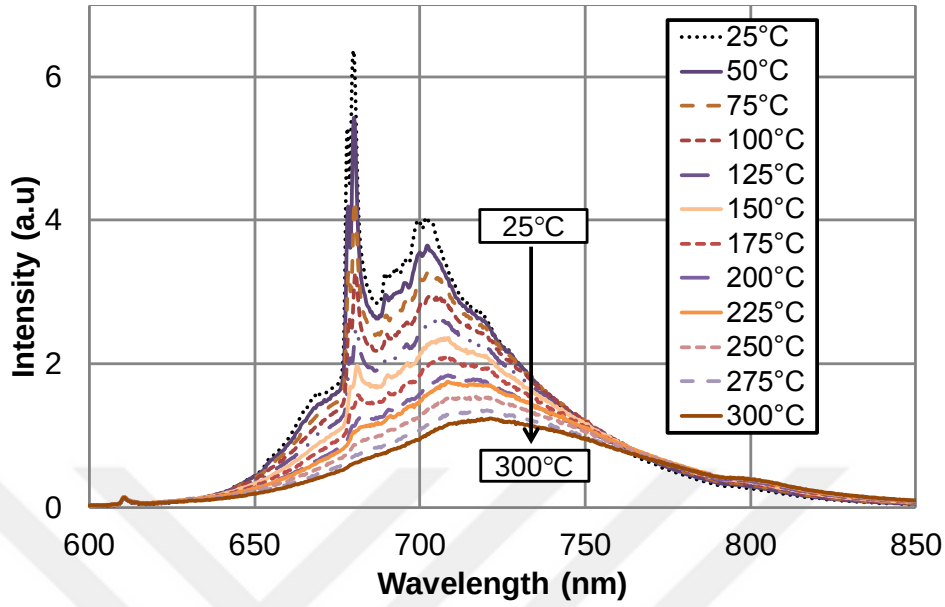


*Fig. 2.3 Measured emission spectra of the Alexandrite crystal between 25°C and 300°C.*

The measured wavelength-dependent emission spectra of the Alexandrite crystal around 700 nm are shown in Fig. 2.3 as a function of temperature between 25 °C to 300 °C. We first note that the strength of the fluorescence spectrum (the number of photons emitted at each wavelength) decreases with increasing crystal temperature. This is mainly due to the reduction in the fluorescence lifetime at increased temperatures as a result of increased non-radiative decay. The decrease in the fluorescence lifetime is stronger than the increase in the effective emission cross section. Therefore, the overall emission strength is reduced at elevated temperatures. Also, the peak of the emission wavelength for the 4-level-laser transition ($^4T_2 \rightarrow {}^4A_2$) shifts from around 700 nm at 25 °C to around 725 nm at 300 °C. A much smaller shift was also observed in the peak emission wavelength of the R-lines (emission resulting from the transition from the $^2E$ ($R_{1/2}$) level to the ground state) [81, 82]. Furthermore, the emission strength of the R-lines decreases with increasing temperature. For example, the sharp-line structures around 680 nm vanish at elevated temperatures of 275 °C and 300 °C. Due to the enhanced phonon dynamics, at these temperatures, the effective emission cross section of the $^4T_2$ transition is much higher than the $^2E$ level.

### 2.3 Continuous-wave lasing results

In this part, we discuss the continuous-wave, single-mode diode-pumped Alexandrite laser results. Fig. 2.4 shows the measured output power as a function of absorbed pump power of the Alexandrite laser at room temperature, using five different output couplers with transmissions ranging from 0.1% to 1.7%. All the experimental data in the following subsections were taken by using the 0.2% Cr-doped, 10-mm-long Alexandrite crystal. At the pump wavelength of 635 nm, the Alexandrite crystal absorbed 95% of the incident pump beam. The laser wavelength was around 760 ± 10 nm for each output coupler. The FWHM (full width at half maximum) linewidth of the laser output was measured to be around 3 nm. The laser output beam had an $M^2$ value of 1.05 with a $TEM_{00}$ beam profile. With 158 mW of absorbed pump power, as high as 48 mW of output power could be obtained with a slope efficiency of 36%, by using 0.5% output coupler. The corresponding optical-to-optical conversion efficiency was 30% for the absorbed pump power. In addition, 29% optical-to-optical efficiency was obtained with respect to the incident pump power. The measured lasing threshold was 28 mW. The threshold pump power measured with the 0.1 % output coupler was as low as 13 mW.

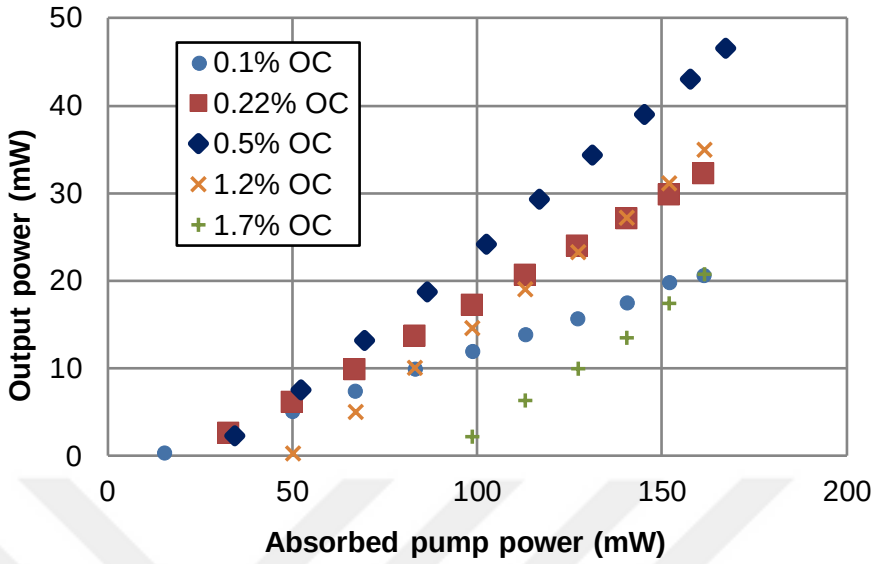


*Fig. 2.4 Measured power efficiency of the cw Alexandrite laser as a function of the absorbed pump power with various output couplers (OCs) between 0.1% and 1.7%.*

We note from Fig. 2.4 that, the slope efficiencies obtained with 0.5% (36%) output coupler is greater than what was obtained with 1.2 % (31%) and 1.7% (29%) output couplers. Similar trends have been observed in tapered diode pumped continuous-wave Alexandrite lasers [83]. This decrease in the slope efficiency at increased output coupling was unexpected and limited the achieved maxima of the slope efficiencies (36%) and output powers (48 mW) in our study. Due to the Auger-type energy transfer upconversion (known as ETU), a similar phenomenon was also observed in Cr: LiSAF and Cr:LiCAF [84, 85]. There is not any previous study that identified ETU as a responsible energy transfer process in the Alexandrite literature, to the best of our knowledge. Although a detailed investigation is necessary, a possible reason for the decrease in the laser efficiency with output coupling is ETU.

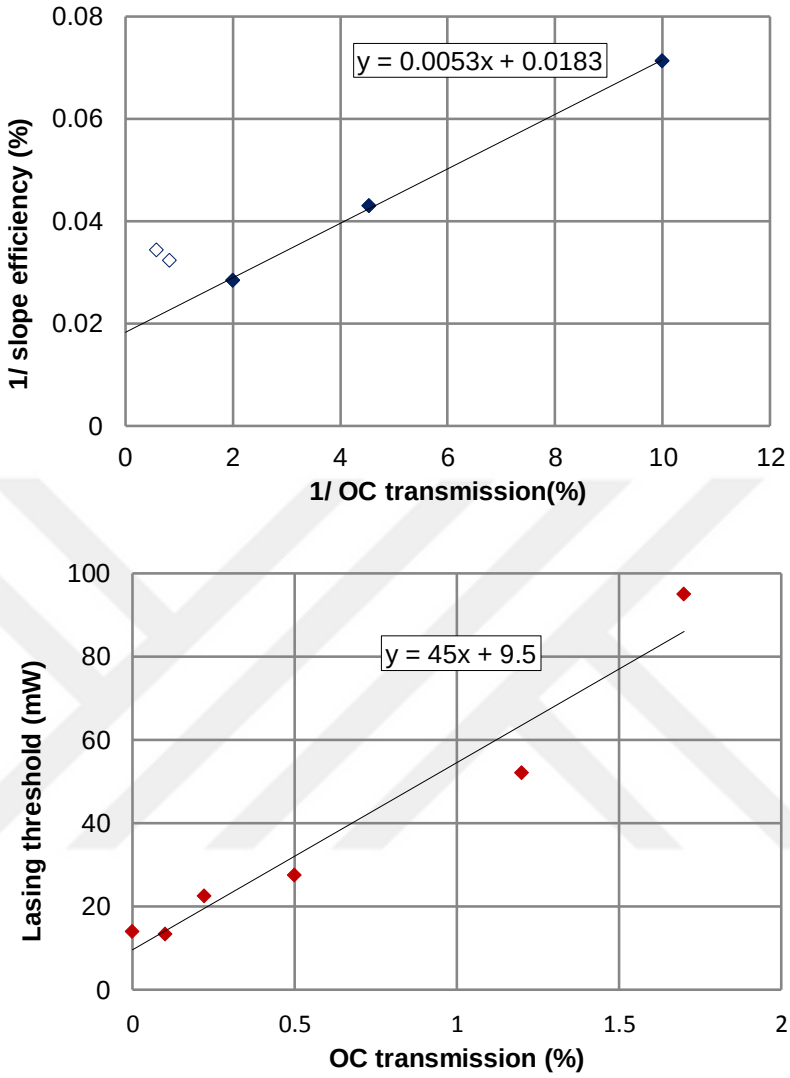


*Fig. 2.5. (a) Measured variation of the 1/slope efficiency as a function of the 1/output coupler transmission (Caird analysis). (b) Measured lasing threshold variation as a function of output coupling (Findlay-Clay analysis).*

Intracavity loss of the Alexandrite laser was estimated by both Caird [86] and Findlay-Clay [87, 88] analyses (Fig. 8). The slope efficiency $\eta$ of the laser can be estimated by using

$$\eta = \left[\left(\frac{h\nu_l}{h\nu_p}\right)\eta_p\left(\frac{\sigma_e - \sigma_{ESA}}{\sigma_e}\right)\right]\frac{T}{T+L} = \eta_0\frac{T}{T+L}, \tag{2.2}$$

in Caird analysis. Here, h is Planck's constant, $\nu_l$ ($\nu_p$) is the laser (pump) photon frequency, $\eta_p$ is the efficiency of pumping, $\sigma_e$ ($\sigma_{ESA}$) is the emission (excited state absorption) cross section, T is the output coupler transmission, L is the total round trip loss of the cavity, and $\eta_0$ is the maximum (intrinsic) slope efficiency that can be obtained at high output coupling. Using this equation and measured values of the slope efficiencies as a function of output coupling we determined the best-fit values of total round trip loss (L) and intrinsic slope efficiency ($\eta_0$) to be (0.3± 0.1) % and (55± 10) %, respectively (Fig. 8 (a)). Due to the unexpected behavior of the high output coupling explained above, we excluded these measured values in the Caird analysis. (The data points excluded in the Caird analysis were shown as hollow diamonds in the Fig. 8 (a)) We determined the total roundtrip cavity loss also by using the measured variation of the threshold pump power as a function of the output coupler transmission (Fig. 8 (b)). The threshold pump power of the laser ($P_{th}$) can be estimated by using the Findlay-Clay analysis [87, 88]:

$$P_{th} = \frac{\pi\left(w_p^2 + w_c^2\right)h\nu_p}{4\left(\sigma_e - \sigma_{ESA}\right)\tau_f \eta_p}\left(2A_g + T + L\right), \qquad (2.3)$$

where $w_p$ ($w_c$) is the pump (cavity) beam waist, $\tau_f$ is the fluorescence lifetime of the upper laser level, and $A_g$ is the ground state absorption of the $Cr^{3+}$ ions. In Alexandrite, the reabsorption loss is negligible around 750 nm. Therefore, $A_g$ can be neglected in this particular case. Using Eq. 2.3, we have determined the best linear fit to the experimental data as $P_{th} \approx 9.5 + 45 \times T$ (in mW units), and hence the round-trip intracavity losses as (0.2± 0.1) %. From these two methods, we end up with similar roundtrip passive losses.

We have further investigated the temperature tuning and the cw laser performance as a function temperature. Figure 2.6 shows the measured variation of the output power as well as laser wavelength as functions of crystal temperature from 25 °C and 200 °C. The laser wavelength was tuned from 760 nm to 805 nm as the temperature of the crystal increased from 25 °C and 200 °C. Referring to the measured temperature-dependent emission spectra (Fig. 2.3), this wavelength shift is expected due to the shift observed in

the peak emission wavelength with increasing temperature. However, the laser wavelength tuning due to the increasing temperature was not continuous and occurred in discrete steps, probably due to a temperature induced birefringence effect. This effect probably created a spectral filter with an effective bandwidth of nearly 10 nm. As the temperature increased from 25 °C and 200 °C, the effective birefringence rotates with a bandwidth of about 10 nm, giving a small detuning of the polarization of the laser circulating in the cavity. The laser beam then observes loss from the crystal surface due to the deviation from TM polarization from the Brewster/Brewster cut gain crystal. As a result, the induced birefringence prevents a continuous wavelength tuning of the laser and discrete wavelength tuning occurred at about every 30 °C-interval when the shift in gain becomes strong enough to allow a jump to the next transmission maxima of the thermally induced birefringent filter. As can be seen from Fig. 2.6, continuous-wave laser power decreased monotonically as the crystal temperature increased. The laser power decreases in discrete steps as the laser crystal temperature increases, similar to what was observed in temperature tuning of the laser wavelength. This is due to the induced birefringence effect at elevated temperatures discussed before. As the polarization of the circulating laser beam rotates due to the birefringence of the gain crystal, it will deviate from the purely TM polarization. Thus, the TE component of the beam will reflect from the surface of the gain medium, causing a decrease in laser power in discrete steps.

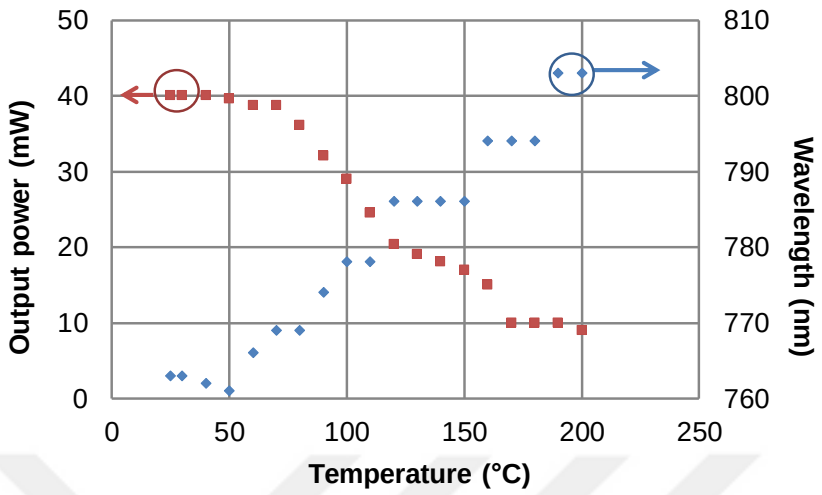


*Fig. 2.6. Measured continuous-wave output power and wavelength of the Alexandrite laser as a function of the crystal temperature. The data were taken with a 0.5 % output coupler at 150 mW of pump power.*

The decrease in the laser performance with increasing temperature was further investigated by measuring the continuous-wave laser efficiencies at different crystal temperatures. Figure 2.7 shows the laser power efficiencies measured at the crystal temperatures of 25 °C, 100 °C, and 200 °C, by using the 0.5 % output coupler. The laser threshold pump power increased abruptly, from 28 mW to 95 mW as the crystal temperature increased from 25 °C to 200 °C. We investigated the temperature dependence of the terms $\sigma_e$ and $\tau_f$ in Eq. 2.3, to understand the increasing trend of the lasing threshold with the threshold pump power. Based on our measurements, the fluorescence lifetime $\tau_f$ was the most sensitive to temperature variations. The fluorescence lifetime of the upper laser level decreased from 265 μs to 80 μs (a factor of 3.3 decrease) when the crystal temperature was elevated from 25 °C to 200 °C. Therefore, the 3.4-fold increase in the threshold pump power was due to the abrupt decrease in the fluorescence lifetime as a function of temperature. Figure 2.8 (a) shows the measured variation of the lasing threshold and the inverse of the fluorescence lifetime as a function of increasing temperature, by normalizing both to their values at room temperature. Although, in

principle, both $\sigma_e$ and $\sigma_{ESA}$ are also temperature dependent, in this case, the variations of the cross sections as a function of temperature were negligible. This effect can be clearly seen in Fig. 2.8 (b) for the emission cross section near 750 nm. The observed decrease in the emission cross section was partly eliminated by temperature tuning to the higher wavelengths at elevated temperatures.

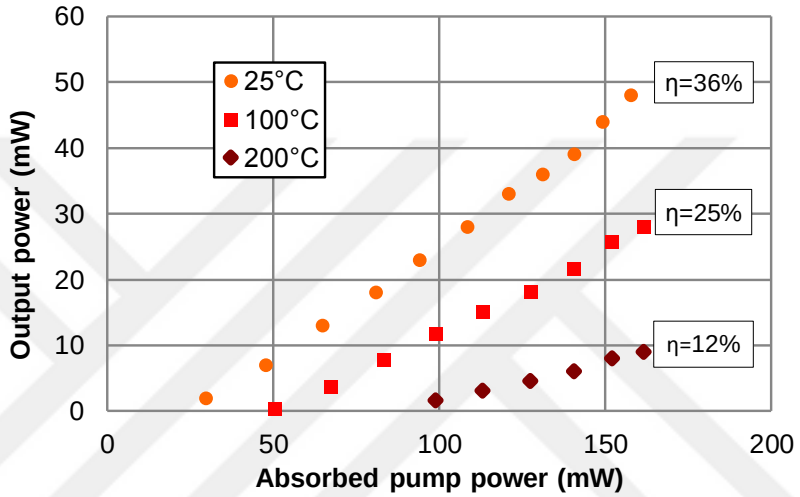


*Fig. 2.7. Measured laser power efficiencies at 25°C, 100 °C, and 200 °C by using the 0.5% output coupler show a monotonic reduction in the slope efficiencies with increasing temperature.*

Figure 2.7 also shows that the measured laser slope efficiencies decrease with increasing temperature, from 36 % to 12 %, as the Alexandrite crystal temperature is increased from room temperature to 200 °C. The observed decrease in the laser power efficiencies with increasing temperature is due to the increased role of excited state absorption at longer lasing wavelengths [79]. As the laser wavelength increases from 760 nm to 805 nm, the quantum efficiency also slightly decreases. This slight change would only cause a decrease of 6% in the efficiencies. The observed (3-fold) decrease in the slope efficiencies could be attributed to the other loss mechanisms such as excited state absorption at longer laser wavelengths.

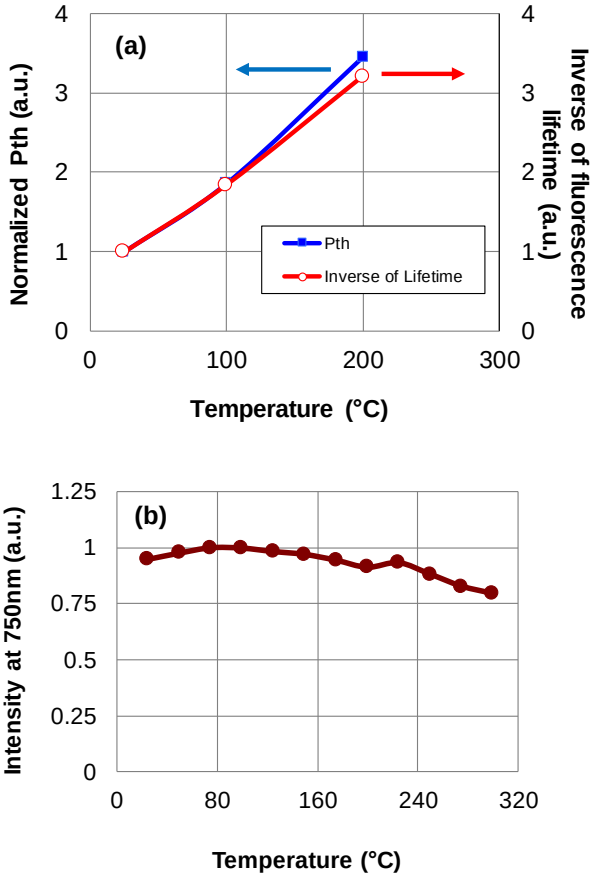


*Fig. 2.8. (a) Measured threshold pump power and the inverse lifetime variations of the Alexandrite crystal as a function of temperature, both normalized to their respective values at 25 ºC. (b) The variation of the measured emission intensities at 750 nm as a function of temperature.*

We also measured the tuning curve of the single-mode diode-pumped Alexandrite laser at different temperatures. Figure 2.9 shows the laser tuning curves with the 0.5% output coupler at an incident pump power of 170 mW. We repeated the tuning experiment for three different temperatures (25 ºC, 100 ºC, and 200 ºC) to determine the change in the tuning wavelengths. The laser output power was lower than what was achieved with the same output coupler before, due to losses caused by the insertion of the birefringent tuning plate. For example, at the free-running wavelength of 760 nm, the output power at room temperature decreased from 48 mW to 34 mW. At room temperature, the laser tuning range was from 736 nm to 795 nm. Since the wavelength-dependent reflectivity

values of the cavity high reflectors start to increase below 735 nm and reach 99.9% at 735 nm, the wavelength tuning range in the short wavelength edge was limited. However, in the literature, laser tuning was obtained at wavelengths as short as 701 nm with a high energy pulsed Alexandrite laser [89]. Further studies are needed with broader bandwidth mirrors to investigate the tuning range of the Alexandrite laser on the short wavelength side. Note that, the excited state absorption and reabsorption losses are also limiting factors for the tuning at short wavelengths [90].

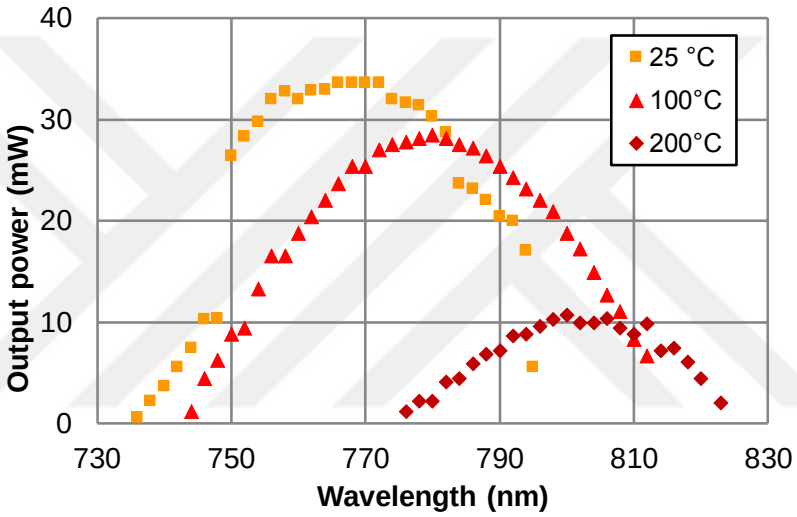


*Fig. 2.9 Measured tuning curves of the cw Alexandrite laser at different crystal temperatures of 25°C, 100°C, and 200°C by using the 0.5% output coupler. The pump power was 170 mW.*

At room temperature, the maximum measured output wavelength was 795 nm. In the earlier studies, a maximum lasing wavelength of 816 nm was reported during tuning experiments [83]. The limited available pump power is possibly the main factor in the observed decrease in the room temperature tuning range in comparison with what was reported in earlier studies. However, by increasing the temperature of the Alexandrite crystal to 200 °C, the tuning limit at longer wavelength was 823 nm. A maximum tuning wavelength of 858 nm was reported earlier by elevating the Alexandrite temperature to the 513 °C [80].

### 2.4 Self-Q-switched operation of Alexandrite laser

In this part, the self-Q-switched operation of the Alexandrite laser will be described briefly. When the laser cavity was aligned to provide the maximum output power, the Alexandrite was operational in the pure cw regime, based on the temporal output profile measured with a fast photodetector. The temporal characteristics recorded with the photodetector are shown in Fig. 2.10, demonstrating the stable laser output, where the relative intensity noise of the laser output was around 3%. However, when the separation between the curved mirrors (CM1 and CM2 in Fig. 2.1) was slightly changed pulsed output of the laser was observed. This phenomenon, observing pulsation without any insertion of a modulator in the cavity, is known as self-Q-switching (SQS) and first reported in 1968 [91]. In the SQS regime, the pulsation occurs due to a modulation inside the gain medium without any further need of any modulator in the laser cavity.

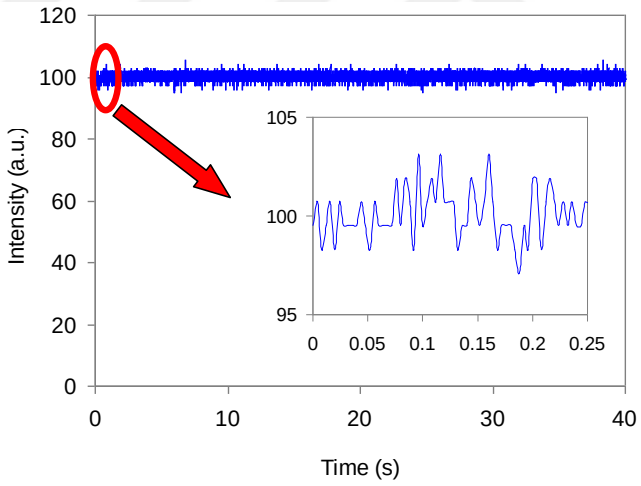


*Fig. 2.10 Measured temporal characteristics of the Alexandrite laser output in the cw regime shows a relative intensity noise about 3%.*

The typical measured temporal characteristics of the Alexandrite laser, when the SQS operation takes place is shown in Fig. 2.11. The data were taken with 0.5% output coupler at the maximum incident power available. For this case, the laser produced 7-μs pulses at 21 kHz repetition frequency. The average laser output power was 30 mW, which corresponds to a 1.4 μJ pulse energy and 210 mW of peak power. We note here that, the

self-Q-switched laser generated quite stable pulses. The shot to shot change in the pulse energy and pulse width was relatively small. The laser pulse widths varied from 5 μs to 15 μs and pulse repetition frequencies in the 10 kHz-35 kHz range for different SQS regime points. For Q-switching, pulse widths and repetition frequencies depend on the pumping level and the total round trip losses in the cavity. Furthermore, the ($TEM_{00}$) profile of the single-mode output of the cw laser transformed into a beam containing higher order transverse modes. In Fig. 2.11 (right), a typical self-Q-switched laser output profile is displayed. In the SQS operation of the $Cr^{3+}$:LiCAF laser, a broadening in the optical spectrum of the output was reported [92]. In our case, the width of the optical spectrum remained unchanged at about 3 nm (FWHM) near the central wavelength of 760 nm.

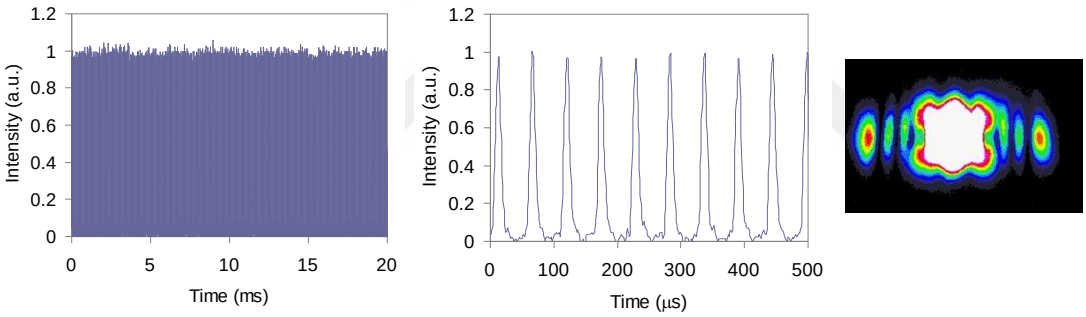


*Fig. 2.11: (Left and Middle) Measured temporal characteristics of the self-Q-switched laser output of the Alexandrite laser at different time scales. The pulse width and the SQS repetition rate were measured to be 7 μs and 21 kHz, respectively. (Right): Measured beam profile of the laser output in the self-Q-switched operation. These are typical for each measurement and may vary at different SQS operation points. An overexposed beam profile was chosen intentionally to show the low-intensity higher order modes.*

In the earlier literature, SQS regime of operation was encountered with various gain media including $Nd^{3+}$:YAG [93], ruby [94], $Cr^{3+}$:LiSAF [95] and $Cr^{3+}$:LiCAF [92] lasers. Self-Q-switching has also been reported in Alexandrite gain media [96] under other names such as “spiking” [97], and “self-pulsation” [98]. The underlying principles of self-Q-switching can be different for each gain medium and were not understood well in

the literature. For trivalent-chromium-doped gain media, the mechanism of SQS was explained as a time-dependent induced lensing inside the gain medium causing a nonlinear loss originating from the refractive index change induced by the population inversion [95, 99-101]. For Alexandrite gain media, the reason for self-Q-switching was connected to the interplay between the number of laser photons and lattice phonons. The ions were excited to the laser level from the storage level, $^2$E at the cost of phonon transitions, and hence the number of generated photons increased. Furthermore, the pumping from ground level manifold to the $^2$E storage level is slower than the transition from the $^2$E storage level to the upper laser level. Therefore, the laser output becomes pulsed. Also, the pulsing regime was found to depend on pump wavelength, pump intensity and cavity losses [98, 102-104].

SQS can be useful for obtaining high peak powers by generating microsecond-long pulses from Alexandrite gain media. This is important for applications such as remote sensing, material processing, nonlinear harmonic generation and range finding. However, generation of SQS-pulses can also make it challenging to obtain long-term stable cw or cw mode-locked operation in these lasers. In our experiments, SQS was harmful to generating long-term pure cw operation which was stable for only 5-10 minutes. Beyond this time, SQS operation would start, probably due to mechanical or thermal perturbations, and realignment was necessary to maintain a stable, pure cw laser output. We note that SQS was not the main intended goal of diode-pumped Alexandrite study and further investigation is needed to fully understand the behavior of SQS.

### 2.5 Conclusions

In this study, we have investigated, in detail, the experimental demonstration of single-mode diode-pumped, continuous-wave and self-Q-switched operation of an efficient and low-threshold Alexandrite laser. The Alexandrite laser cavity was pumped with only one single-mode diode which provides up to 170 mW of pump power centered at 635 nm. Maximum output power of 48 mW and a slope efficiency of 36% were demonstrated. The lowest measured threshold pump power was 13 mW. By using Caird-

type and Findlay-Clay-type loss analyses, round trip losse of the cavity was estimated around 0.25 %. The cw laser output was tuned at different crystal temperatures, resulting in tuning ranges from 736 nm to 795 nm at 25 °C, and from 776 nm to 823 nm at 200 °C. SQS operation was also observed during the experiments by slight misalignment of the cavity mirrors or by changing the curved mirror separation in the cavity. The pulses generated during the SQS operation had pulse widths of between 5 μs and 15 μs and repetition frequencies in the 10-35 kHz range. This is one of the most compact and low-cost Alexandrite laser efficiently operated around 760 nm in the literature and has the potential to be used in several applications.

# Chapter 3

## Continuous-wave 2.3-μm $Tm^{3+}$:YLF lasers

In this chapter, continuous-wave operation of 2.3-μm $Tm^{3+}$:YLF lasers pumped by using a continuous-wave $Ti^{3+}$:sapphire laser and two different diode lasers will be investigated. First, a continuous-wave, tunable, and narrow-line $Ti^{3+}$:sapphire laser was used to measure the excitation spectrum, and behavior of the absorption saturation of 1.5 at. % $Tm^{3+}$:YLF gain medium will be explained. In addition, continuous-wave laser performance results will be shown including slope efficiencies and tuning range between 2273 nm to 2365 nm $Ti^{3+}$:sapphire pump laser. Further, the diode-pumped operation of the $Tm^{3+}$:YLF lasers at 2.3 μm will be investigated in detail. By using a 120-mW laser diode at 792 nm, the low threshold operation of the $Tm^{3+}$:YLF laser was obtained with as low as 25 mW of pump power. For the 250-mW laser diode, a detailed investigation of slope efficiencies and threshold pump powers were provided for eighteen different effective output couplings. For this pumping scheme, the incident threshold pump power at 0% OC was measured to be 4 mW.

### 3.1 Experimental setup

We first constructed a tunable, narrow-line, and continuous-wave $Ti^{3+}$:sapphire laser to investigate the continuous-wave characteristics of the $Tm^{3+}$:YLF laser at 2.3 μm. The $Ti^{3+}$:sapphire laser was built by using a 5-W continuous-wave pump source at 532 nm (OPUS MPC 6000, Laser Quantum) (Fig. 3.1 (a)). The green pump laser was focused inside a Brewster-cut, 10-mm $Ti^{3+}$:sapphire crystal by using a converging lens (L1) of focal length 75 mm. The crystal figure of merit was greater than 250 and absorbed 92% of the 532-nm pump beam. The laser cavity was set up with x-folded four mirrors

including two curved high reflectors each with a radius of curvature of 70 mm (M1 and M2) and a flat high reflector (M3) and a flat output coupler mirror (M4) with 15% transmission at 800-nm center wavelength. A pair of Brewster-cut intracavity SF10 prisms (P1 and P2) were included in the $Ti^{3+}$:sapphire cavity to tune the output wavelength and to reduce the pump linewidth to 0.08 nm (Fig. 3.1 (a) and (b)). An optical spectrum analyzer (Anritsu MS9740A) with a resolution of 0.07 nm and bandwidth of 100 Hz was used to measure the linewidth. At the maximum input power of 5 W at 532 nm, the $Ti^{3+}$:sapphire laser provided 930 mW output power at 780 nm. The tuning range of the $Ti^{3+}$:sapphire laser extended from 694 nm to 846 nm. The $M^2$ value of the $Ti^{3+}$:sapphire output beam was further determined to be 1.5 by using the knife edge technique.

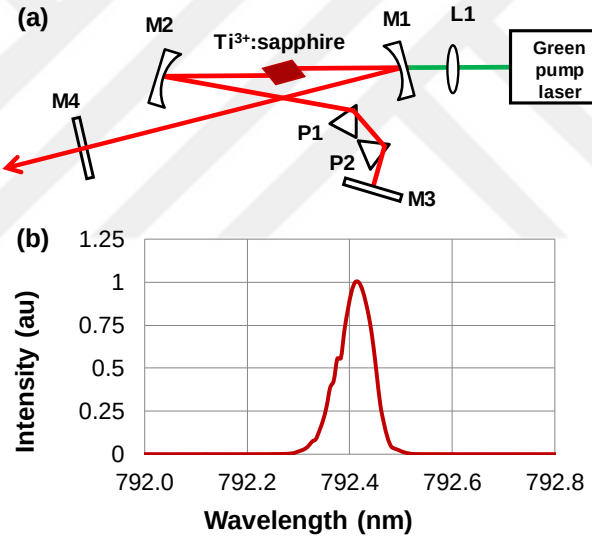


*Fig. 3.1 (a) Schematic of the tunable and narrow-line $Ti^{3+}$:sapphire laser pumped by using a 5-W green laser. (b) The output spectrum of the $Ti^{3+}$:sapphire pump laser. The full width at half maximum (FWHM) linewidth was 0.08 nm.*

Figure 3.2 shows the experimental setup of the $Ti^{3+}$:sapphire pumped continuous-wave $Tm^{3+}$:YLF laser. The $Ti^{3+}$:sapphire laser described before and shown in Fig. 3.1 was lumped into a box to avoid redundancy in Fig. 3.2. The output of the $Ti^{3+}$:sapphire pump laser was focused inside the 9-mm-long, Brewster-cut 1.5 at. % $Tm^{3+}$:YLF crystal

by using a converging lens (L2, f=75mm). The laser crystal absorbed the 78% and 68% of the pump beam at 780 nm and 792 nm respectively. The $Tm^{3+}$:YLF crystal was mounted in a temperature-managed copper holder at 21°C. A standard 4-mirror, x-cavity was built by using two curved high reflectors (M3 and M4, each with a radius of curvature of 100 mm), a flat high reflector (M5) and an output coupler mirror (OC). In our experiments, output coupler mirrors with transmission values of 1% and 3.2% were used. High reflector mirrors had coatings with reflectivity >99.8% between 2200-2500 nm and the input mirror (M3) coupled 85% of the pump beam into the $Tm^{3+}$:YLF laser resonator. The arm lengths of the $Tm^{3+}$:YLF cavity were 49 cm (M5 arm) and 65 cm (OC arm), giving an estimated beam waist of 39 μm in the gain crystal.

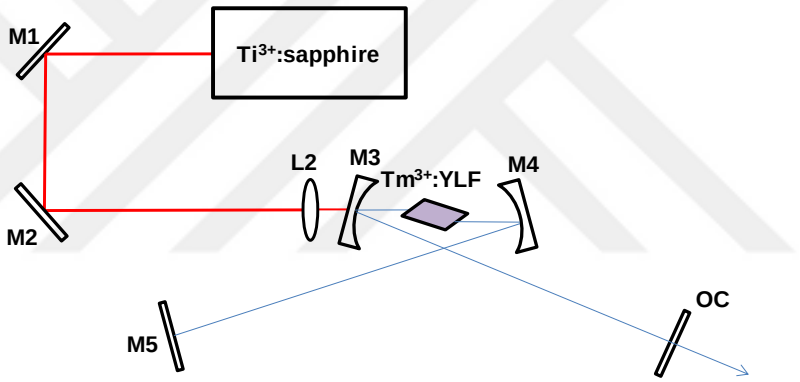


*Fig. 3.2 Schematic of the continuous-wave $Tm^{3+}$:YLF laser pumped by a $Ti^{3+}$:sapphire laser and operating at 2.3 μm.*

## 3.2 Absorption saturation and lasing characteristics of the 1.5% $Tm^{3+}$:YLF crystal

Before constructing the resonator, first the absorption saturation behavior of the $Tm^{3+}$:YLF crystal was investigated. Referring to Fig. 3.2, only the input lens and the input curved mirror (L2 and M3) were used in these measurements before the $Tm^{3+}$:YLF crystal. Two sets of experimental data were recorded. In the first set, the $Tm^{3+}$:YLF crystal was translated to the location which maximizes the pump transmission. The

transmission of the crystal was then measured as a function of the incident pump power. In the second set of measurements, the incident pump power was kept constant at 930 mW and the variation of the crystal transmission was measured as a function of the relative crystal position. In these measurements, the wavelength and beam waist of the pump beam were 792.4 nm and 28 μm, respectively. These saturation data were shown in Figs. 3.3 (a) and (b).

We used a rate equation model to investigate the absorption characteristics of the $Tm^{3+}$:YLF crystal by accounting for the absorption saturation and excited-state absorption of the pump beam. As discussed in Ref. [105], the cross sections for ground-state absorption ($\sigma_a$) and excited-state absorption ($\sigma_{esa}$) of the $Tm^{3+}$:YLF crystal can be determined by using the differential equation [105]:

$$\frac{dP}{dz} = -\alpha_{p0} P \int_0^{\infty} dr 2\pi r \phi \left( \frac{1 + f_p \frac{P\phi}{I_{sa}}}{1 + \frac{P\phi}{I_{sa}}} \right). \quad (1)$$

Here, $P$ is the pump power, $\sigma_a$ is the ground-state absorption cross section, $\alpha_{p0}$ is the small-signal differential absorption coefficient ($\alpha_{p0} = N_T \sigma_a$, $N_T$=total ion density), $f_p = \sigma_{esa}/\sigma_a$, $\sigma_{esa}$ is the excited-state absorption cross section at the pump wavelength, $r$ is the radial coordinate, $I_{sa}$ is the saturation intensity given by $I_{sa} = h\nu/\sigma_a \tau_f$, and $\phi$ is the normalized power distribution of the Gaussian beam.

This model was used to analyze the two sets of absorption saturation data depicted in Figs 3.3 (a) and (b). In the first case (Fig. 3.3 (a)), the beam waist position was fixed in the crystal and the crystal transmission was measured as a function of the incident pump power. The parameters $\alpha_{p0}, \sigma_a$, and $f_p$ were then varied to obtain the best fit between the experimental data and the rate equation model given in Eq. 1. The best-fit values of $\alpha_{p0}, \sigma_a$, and $f_p$ were determined to be $\alpha_{p0} = 1.3 cm^{-1}$, $\sigma_a = 0.93 \times 10^{-20} cm^2$, and $f_p = 0.04$. Here, we use the average of the fluorescence lifetime values ($\tau_f = 12.5 ms$)

reported in the literature for the $^3F_4$ state [72, 106-110]. In the second case (Fig. 3.3 (b)), the incident pump power was kept constant at 930 mW and the crystal transmission was measured as a function of the relative crystal position (in other words, as a function of the beam waist location within the crystal). Best fit between the experimental data shown in Fig. 3.3 (b) and the rate equation model was obtained for $\alpha_{p0} = 1.4\,cm^{-1}$, $\sigma_a = 0.6\times10^{-20}cm^2$ and $f_p = 0$. The average value of $\sigma_a$ came to $\sigma_{a,avg} = 0.77\times10^{-20}cm^2$, in good agreement with the value of $\sigma_a = 0.65\times10^{-20}cm^2$ determined from $\sigma_a = \alpha_{p0}/N_T$, where $N_T = 2.08\times10^{-20}cm^{-3}$ for the 1.5 at. % $Tm^{3+}$:YLF. Also note that, the analysis of the saturable absorption data predicts a negligible level of excited-state absorption at the pump wavelength since the average value of $f_p$ was very small (0.02).

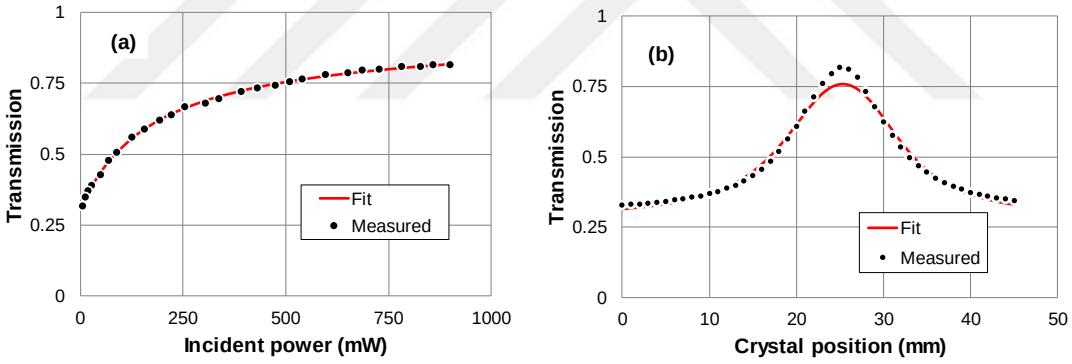


*Fig. 3.3 Measured and fit variation of the $Tm^{3+}$:YLF crystal transmission at 792.4 nm as a function of (a) the incident pump power when the beam waist location was fixed near the center of the crystal to maximize saturation and, (b) the relative crystal position when the incident pump power was kept constant at 930 mW.*

Following the saturation characterization, the excitation spectrum of the $Tm^{3+}$:YLF crystal was determined by using the $Ti^{3+}$:sapphire laser as the pump source. The excitation spectrum displayed in Fig. 3.4 shows the measured output power of the $Tm^{3+}$:YLF laser at 2305 nm as a function of the pump wavelength (left axis, dotted

curve). The output coupler transmission was 1%. Also shown in the same figure is the measured variation of the $Ti^{3+}$:sapphire output power over the same wavelength range (right axis, continuous curve). In these measurements, the $Ti^{3+}$:sapphire wavelength was varied in increments of 0.5 nm. The 2.3-µm laser operation could be achieved with pump wavelengths from 763 nm to 807 nm. In this wavelength range, the available input pump powers remained above 910 mW. As can be seen from the figure, the $Tm^{3+}$:YLF laser can be efficiently excited by using the absorption bands centered at 780.4 nm and 792.4 nm, where the small signal absorption of the $Tm^{3+}$:YLF crystal was 78% and 68%, respectively. With 930 mW of input pump power, the $Tm^{3+}$:YLF laser yielded 109 mW and 94 mW of output power at the pumping wavelengths of 780.4 nm and 792.4 nm.

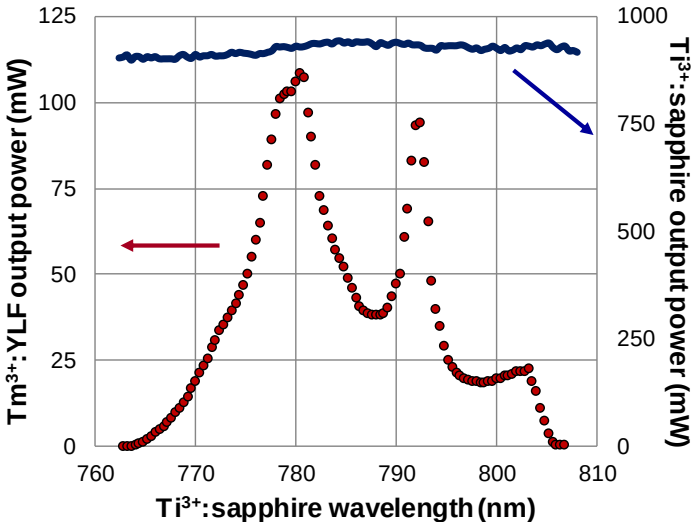


*Fig. 3.4 $Ti^{3+}$:sapphire tuning curve (right axis, continuous curve) and the corresponding $Tm^{3+}$:YLF laser excitation spectrum (left axis, dotted curve) with 1% OC.*

Figure 3.5 shows the measured power efficiencies of the $Tm^{3+}$:YLF laser pumped by the $Ti^{3+}$:sapphire laser at 780 nm and 792 nm. Output couplers with 1% and 3.2% transmission were used. For both pumping wavelengths, higher power performance was obtained with the 1% OC. In particular, as can be seen from Fig. 3.5 (a), when pumped at 780 nm, the $Tm^{3+}$:YLF laser yielded power efficiencies of 12.8 % and 7.7 % at 2305 nm with 1 % and 3.2 % output couplers, respectively. Furthermore, 792-nm excitation

resulted in 9.4 % and 6.3 % slope efficiencies for 1 % and 3.2 % output couplers (Fig. 3.5 (b)). With the 1 % output coupler, as high as 119 mW (92.5 mW) of output power was obtained with 958 mW (998mW) of pump power at 780.4 nm (792 nm).

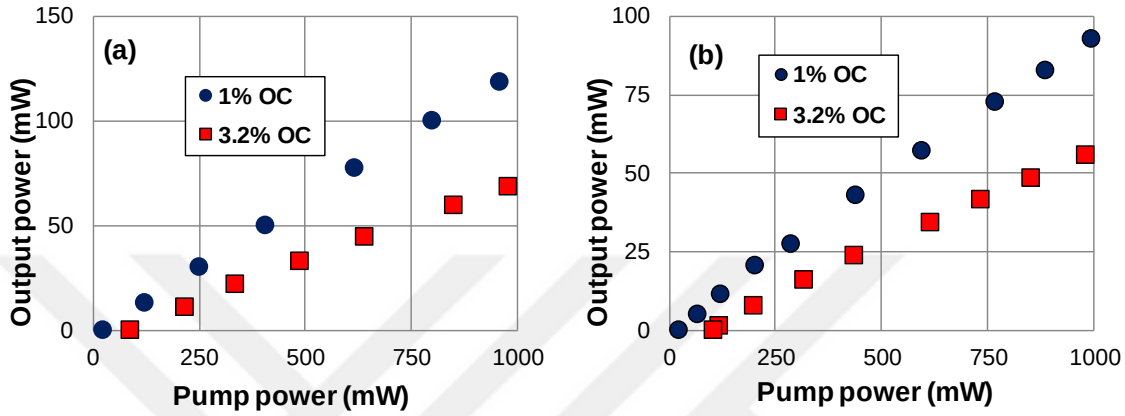


*Fig. 3.5 Measured power efficiencies of the $Tm^{3+}$:YLF laser pumped with the $Ti^{3+}$:sapphire laser at (a) 780 nm and (b) 792 nm with 1% and 3.2% output couplers. The output wavelength was 2305 nm.*

In the tuning experiments, a 5-mm quartz tuning plate was included in the cavity. The measured variation of the output power as a function of the output wavelength is shown in Fig. 3.6. With a constant input power of 985 mW (780 nm), the tuning range of the laser extended from 2273 nm to 2365 nm.

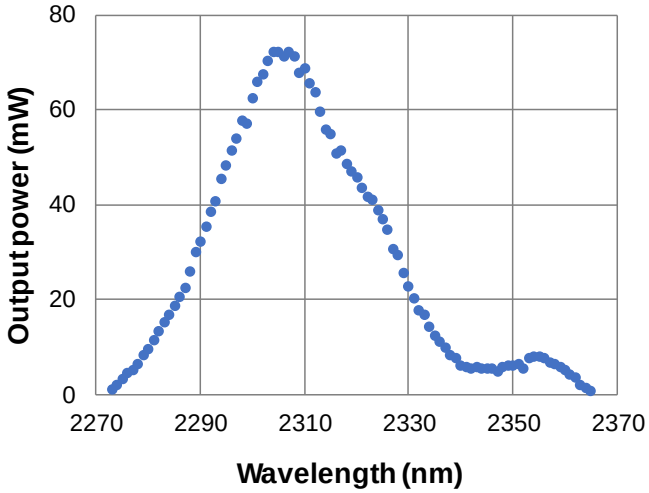


*Fig. 3.6 Measured tuning curve of the $Ti^{3+}$:sapphire pumped $Tm^{3+}$:YLF laser with 1 % output coupler. A 5-mm quartz plate was used for tuning.*

### 3.3 Diode pumped, continuous-wave 2.3-μm $Tm^{3+}$:YLF laser results

In this section, we describe low-threshold and diode-pumped operation of the 2.3-μm $Tm^{3+}$:YLF laser by using two different diode pumping configurations. In the first configuration, we demonstrated low-threshold 2.3-μm laser operation by using a low-cost, single-mode laser diode with a maximum output power of about 120 mW at 792 nm. Figure 3.7 (A) shows the first pumping configuration employing a single-mode, 785-nm, AlGaAs laser diode. A micro-lens was assembled near the diode facet to provide a circular output beam profile (Fig. 3.7 (A)). At the maximum driving current of 160 mA and case temperature of 45 °C, the laser diode produced 120 mW at 792 nm. The measured linewidth of the diode laser output was 0.09 nm, close to the resolution limit (0.07 nm) of the optical spectrum analyzer (Anritsu MS9740A). The measured spectrum of the pump diode is further shown in the inset of Fig. 3.7 (A). The $M^2$ of the laser beam was measured as 1.1. The output of the diode laser was then collimated using an anti-reflection (AR) coated aspherical lens (L1) with a focal length of 4.5 mm. The $Tm^{3+}$:YLF laser cavity was similar to what was described in detail before in Section 3.1.

In the second pumping configuration, a diode laser producing a maximum power of 400 mW at 785 nm was used (Fig. 3.7 (B)). The laser could provide up to 250 mW of output power at 792 nm and 46 °C with 500 mA of driving current. An AR coated 2× anamorphic prism pair was used to obtain a circular beam. The measured linewidth and $M^2$ were 0.08 nm and 1.1, respectively. The second pumping configuration was used to measure the variation of the threshold pump powers and slope efficiencies as a function of output coupler transmission. In these measurements, an additional 6-mm-thick, parallel polished YAG substrate was inserted at Brewster's angle in the OC arm of the $Tm^{3+}$:YLF laser. The effective output coupling of the laser was then varied by tilting the YAG etalon from Brewster incidence. The corresponding effective output coupling was determined by measuring the powers P1, P2, and P3 of the output beams shown in Fig. 3.7 (B).

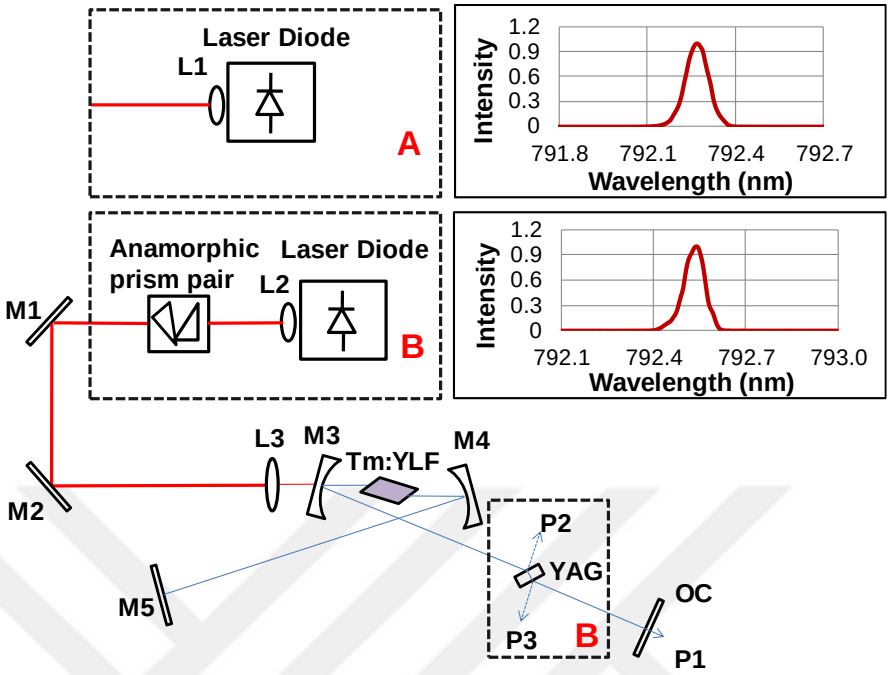


*Fig. 3.7 Diode pumping configurations of the 2.3-μm $Tm^{3+}$:YLF laser by using (A) a 120-mW, single-mode laser diode, and (B) a 250-mW laser diode. The insets further show the measured spectral output of each pump diode.*

By using the 120-mW pump diode, we first demonstrated low threshold operation of the $Tm^{3+}$:YLF laser at 2305 nm. As can be seen from Fig. 3.8, as high as 10.5 mW of output power was obtained with 119 mW of pump power. The measured slope efficiency and threshold pump power were 11.4 % and 25 mW, respectively, when the 1% output coupler was used. For this pumping configuration, the available pump power was not sufficient to obtain lasing with the 3.2% output coupler.

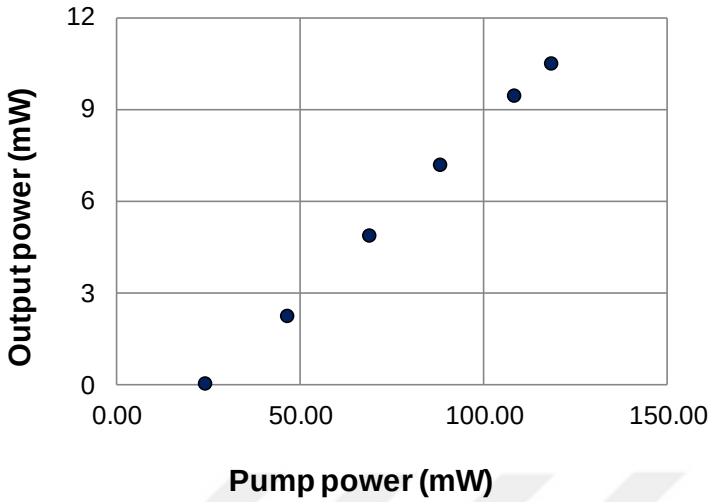


*Fig. 3.8. Measured power efficiency of the 2305-nm $Tm^{3+}$:YLF laser pumped with the 120-mW diode laser at 792 nm. The output coupler transmission was 1%.*

By using the second pumping configuration, the total output power (P1+P2+P3) was first measured as a function of the effective output coupling at the fixed input power of 250 mW. To obtain output coupling levels below 1 %, the 1 % output coupler was replaced by a high reflector and the calibrated tilt positions of the YAG substrate were used attain the desired effective output coupling. As can be seen from Fig. 3.9, the optimum output coupling was 0.7 %, showing the low gain nature of this gain medium. Also, these measurements showed that lasing could not be obtained at output coupling levels above 7 %.

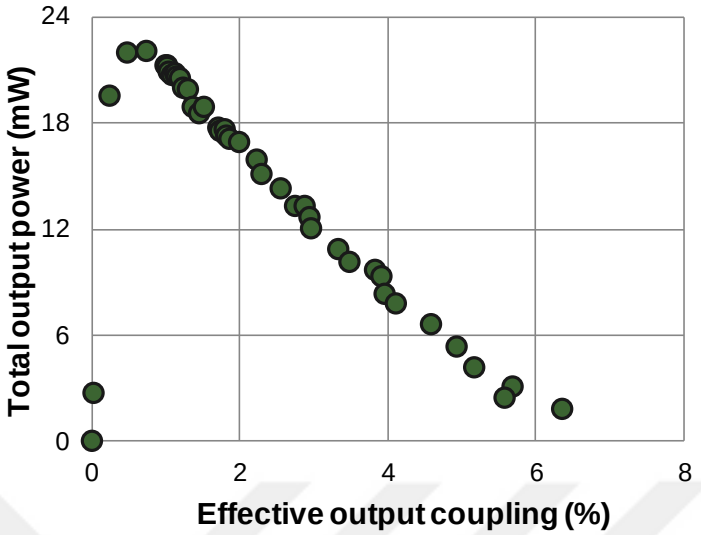


*Fig. 3.9. Measured total output power variation as a function of the effective output coupling. The input pump power was 250 mW.*

Lasing threshold data can be used to determine the round-trip cavity loss (L) of the $Tm^{3+}$:YLF laser and the stimulated emission cross section ($\sigma_e$) for the $^3H_4$-$^3H_5$ transition. For an ideal 4-level laser, the incident threshold pump power can be determined by using the formula [42]

$$P_{th} = \frac{\pi\left(w_p^2 + w_L^2\right)h\nu_p}{4\sigma_e \tau_f \eta_a}(L+T), \tag{2}$$

where, $w_p$ and $w_L$ correspond to the root mean squared spot sizes of the pump and laser beams inside the gain medium. In addition, $\nu_p$ is the pump photon frequency, $\tau_f$ is the fluorescence lifetime of the upper laser level, $\eta_a$ is the small-signal pump absorption, $T$ is the transmission of the output coupler at the laser wavelength, and $L$ is the total roundtrip loss of the cavity. From the ABCD analysis of the pump and cavity beams, $w_p$ and $w_L$ were calculated to be 33 μm and 51 μm, respectively. As can be seen from Eq. 2, the incident threshold pump power is expected to vary linearly with the roundtrip cavity loss (L). Figure 3.10 shows the experimentally measured incident threshold pump power

as a function of effective output coupling (T) for the 2305-nm $Tm^{3+}$:YLF laser. Note that, the measured threshold power shows a departure from the expected linear trend at output coupling levels above 2.5 %. The reason for the increase in the threshold pump power is possibly due to an Auger-type energy upconversion process which results in a nonradiative depletion of the upper laser level. At low output coupling, the intracavity laser intensity is relatively high, leading to enhanced stimulated decay to the lower laser level and reduced nonradiative upconversion. Hence, the unwanted effect of upconversion becomes more pronounced at higher output coupling and gives rise to higher lasing thresholds. In order to determine the roundtrip cavity loss, a linear Findlay-Clay type fit [87] was made to the threshold data at low values of T, as shown by the straight tangent in Fig. 3.10. This gave a best fit value of 0.21% for L, from which the stimulated emission cross section was determined to be $\sigma_e = (0.55 \pm 0.04) \times 10^{-20} cm^2$, which was close to the absorption cross-section value we determined from the saturation measurements. The average stimulated emission cross section value reported in previous studies was $\sigma_e = 1 \times 10^{-20} cm^2$ [30, 72].

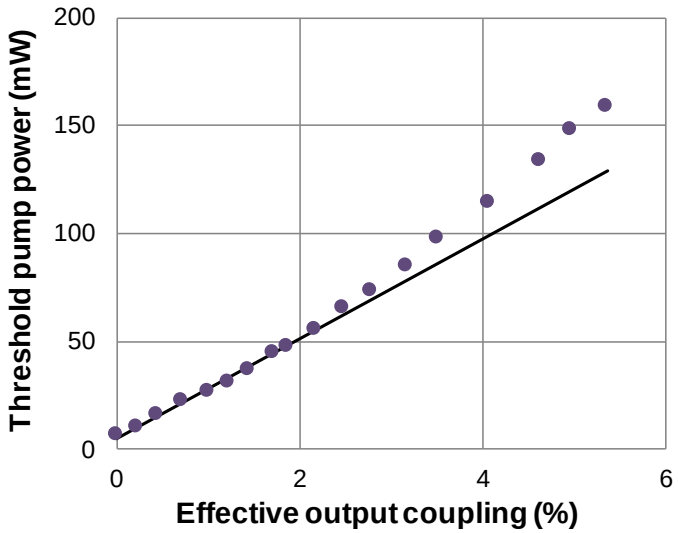


*Fig. 3.10. Measured variation of the incident threshold pump power as a function of the effective output coupling for the 2305-nm $Tm^{3+}$:YLF laser.*

Figure 3.11 further shows the measured power slope efficiencies (with respect to the incident power) as a function of the effective output coupling. In these measurements, the output power of the $Tm^{3+}$:YLF laser at 2305 nm was first recorded as a function of the incident pump power at eighteen different output coupling levels. A linear best-fit was then applied to each data set to determine the slope efficiency. Note that, beyond the optimum output coupling of approximately 0.7 %, the slope efficiency showed a decrease with increasing output coupling. This is contrary to what is typically observed in 4-level laser systems where the slope efficiency given by

$$\eta = \frac{\lambda_p}{\lambda_L}\frac{T}{T+L}\eta_a \tag{3}$$

approaches its maximum value at large output coupling levels [111]. In Eq. 3, $\eta$ is the slope efficiency with respect to the incident power, $\lambda_p$ and $\lambda_L$ are the wavelengths of the pump and laser beams. As discussed above, a possible cause of the decrease in the power slope efficiency beyond 0.7% output coupling is the nonradiative energy upconversion process. Also shown in Fig. 10 is the ideal variation of the slope efficiency, calculated by using Eq. (3) and L=0.21%.

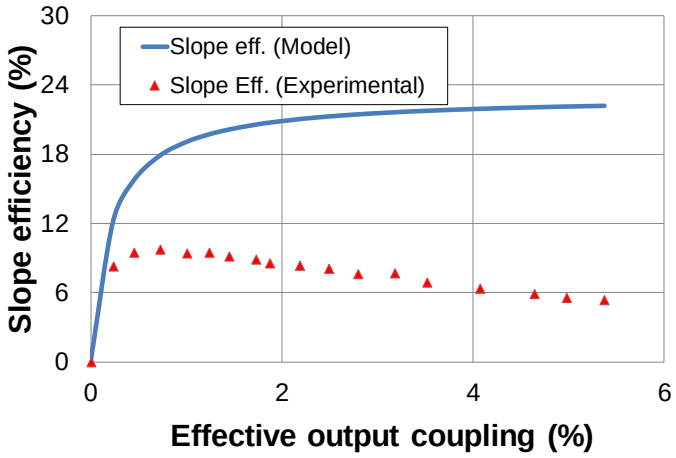


*Fig. 3.11. Measured power slope efficiency (solid triangles) of the 2305-nm $Tm^{3+}$:YLF laser as a function of effective output coupling. The continuous curved shows the expected variation from Eq. (3) by assuming a loss level of L=0.21%.*

### 3.4 Conclusions

In conclusion, we have performed a thorough investigation of a continuous-wave 2.3-μm $Tm^{3+}$:YLF laser pumped by using a cw $Ti^{3+}$:sapphire laser and two different laser diodes. By using the $Ti^{3+}$:sapphire pump laser, the excitation spectrum was measured and the optimum pumping wavelength was determined to be 780 nm. From the absorption saturation measurements, the average value of the stimulated absorption cross section was further determined to be $\sigma_a = 0.77 \times 10^{-20} cm^2$. A low cost, low threshold 2.3-μm $Tm^{3+}$:YLF laser configuration was then demonstrated by using a 120-mW laser diode operating at 792 nm. Here, as high as 10.5 mW of output power could be obtained at 2305 nm with a slope efficiency of 11.4 %. With a second 250-mW pump diode, we performed a detailed investigation of how the threshold pump power and laser slope efficiency vary as a function of output coupler transmission. These measurements indicated the highest laser slope efficiency of about 10% was achieved at the output coupling of 0.7 %. Further increase in output coupling resulted in a decrease in the laser slope efficiency possibly due to losses arising from nonradiative upconversion processes. Threshold power data further yielded a best-fit value of $\sigma_e = (0.55 \pm 0.04) \times 10^{-20} cm^2$ for the stimulated emission cross section. Our results show that low-cost, low-threshold, diode-pumped $Tm^{3+}$:YLF lasers operating near 2.3 μm have the potential of becoming versatile sources of mid-infrared radiation.

# Chapter 4

# Passive Q-switched operation of $Tm^{3+}$:YLF laser at 2.3 μm

In this chapter, we will describe the first pulsed operation of the 2.3-μm $Tm^{3+}$:YLF laser in the literature, to the best of our knowledge [28]. First, we will explain the power performance of the passively Q-switched and continuous-wave output prior to the insertion of the $Cr^{2+}$:ZnSe saturable absorber. Furthermore, we will describe the temporal characteristics of the Q-switched pulses, including the variation of repetition frequency, pulse width, pulse energy, and peak power with pump power. In addition, the estimation of the small-signal loss of the saturable absorber based on passive Q-switching analysis will be presented.

## 4.1 Experimental setup

Figure 4.1 shows the experimental setup of the passively Q-switched 2.3-μm $Tm^{3+}$:YLF laser with a polycrystalline $Cr^{2+}$:ZnSe saturable absorber (SA) within the cavity. The prism tuned and narrow-line $Ti^{3+}$:sapphire laser explained in Section 3.1 was used to pump the $Tm^{3+}$:YLF laser cavity. The $Ti^{3+}$:sapphire laser was tuned to 780 nm to achieve the maximum small-signal absorption of 78 %. The $Ti^{3+}$:sapphire laser generated 900 mW of output power at 780 nm at the maximum input green pump power of about 5W. In order to adjust the pump power level, a half-wave plate (HWP) and a polarizing beam splitter (PBS) were used. This method ensured that a TM polarized output of the pump source was sent to laser crystal without changing the thermal lensing, and hence, the beam profile of the $Ti^{3+}$:sapphire laser. The pump beam was sent into a 9-mm, Brewster-cut and 1.5 at. % thulium-doped $Tm^{3+}$:YLF laser crystal by using two flat mirrors (M1 and M2) and a focusing lens of focal length 75 mm (L1). The residual pump beam transmitted from the crystal was retroreflected by using a concave mirror (M5, radius of curvature, ROC=75 mm) to increase the amount of absorbed pump power. An astigmatically compensated x-fold cavity was set up by using four high reflecting curved mirrors (M3-M4, M6-M7 each with a ROC=75 mm)

and a flat output coupler with 1 % transmission (M8). The additional beam waist on the 2.6-mm-long $Cr^{2+}$:ZnSe saturable absorber (SA) was formed by two of the curved mirrors in the high reflector arm. The beam waist on the $Cr^{2+}$:ZnSe SA was estimated to be 21 µm based on the ABCD analysis of the cavity.

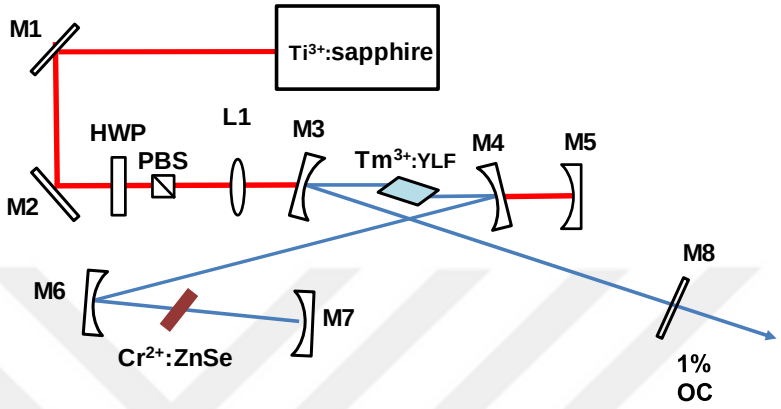


*Fig. 4.1 Experimental setup of the 2.3-µm passively Q-switched $Tm^{3+}$:YLF laser based on the use of a $Cr^{2+}$:ZnSe saturable absorber.*

### 4.2 Continuous-wave and Q-switched power performance results

We first set up a free-running cavity, where we do not insert the $Cr^{2+}$:ZnSe saturable absorber in the cavity. In this free-running continuous-wave laser cavity, 102 mW of output power was obtained with 880 mW of pump power. The output power at 2.3 µm increased to 150 mW by double pumping at the same input pump power. The measured output power variation with incident power is shown in Fig. 4.2 (a) for single- and double-pumped laser cavities. When the output coupler transmission was 1%, the slope efficiencies were 14 % and 19 % and the threshold pump powers were 114 mW and 100 mW for the cases of single and double pumping, respectively. The roundtrip loss of the cavity without the $Cr^{2+}$:ZnSe SA was found to be 0.3 % based on the measured threshold pump power data with output couplers of different transmission levels [87].

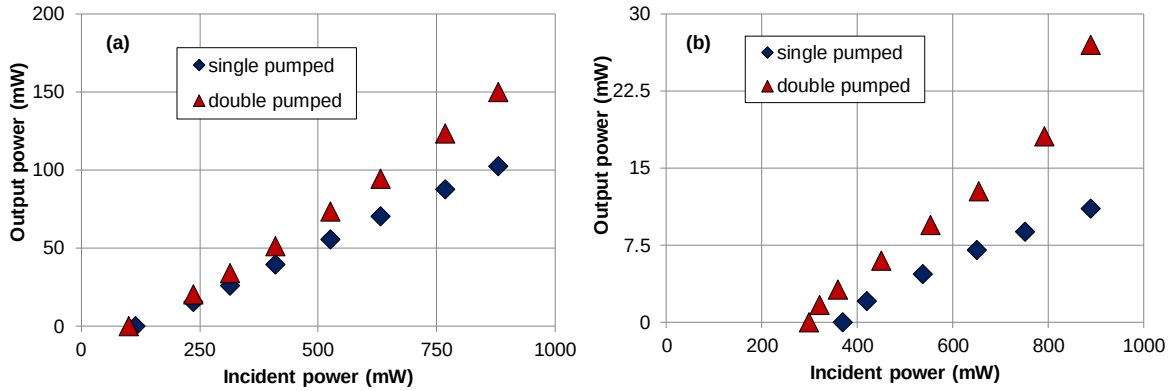


*Fig. 4.2 Measured variation of the average output power as a function of the incident pump power (before lens L1) for the (a) cw-$Tm^{3+}$:YLF laser, and (b) pulsed $Tm^{3+}$:YLF laser passively Q-switched with a of $Cr^{2+}$:ZnSe saturable absorber in the cavity. Data for single and double pumping cases are shown in each graph.*

The $Cr^{2+}$:ZnSe saturable absorber was placed in the additional waist formed in between mirrors M6 and M7 at Brewster's angle. Due to the $^5T_2 \rightarrow {}^5E$ transition, the $Cr^{2+}$:ZnSe saturable absorber had 70% absorption at the peak absorption wavelength of 1775 nm. At the laser operation wavelength of 2309 nm, the measured single-pass unsaturated loss of the $Cr^{2+}$:ZnSe saturable absorber was 3.6%. We could not identify the longer-wavelength absorption band due to the Jahn-Teller split $^5T_2$ ground state [112]. Therefore, the residual absorption at 2309 nm was possibly due only to the $^5T_2 \rightarrow {}^5E$ transition. The laser output power decreased from 150 mW (102 mW) to 27 mW (11 mW) for double (single) pumped laser cavity at 890 mW of input pump power, after the insertion of the $Cr^{2+}$:ZnSe saturable absorber. The measured output power variation of the passively Q-switched $Tm^{3+}$:YLF laser is shown in Fig. 4.2 (b). With the insertion of the $Cr^{2+}$:ZnSe in the cavity, passively Q-switched operation was achieved at all pump powers above lasing threshold. The threshold pump powers for the single- and double-pumped cavity were 380 mW and 300 mW, respectively.

### 4.3 Temporal characteristics of the passively Q-switched pulses

Temporal profile of the Q-switched pulse is shown in Fig. 4.3(a), where the measured pulse duration was 1.3 µs for the input pump power of 890 mW. In Fig. 4.3(b), the output spectrum of the passively Q-switched laser is shown. The center wavelength of the output was measured to be 2309 nm.

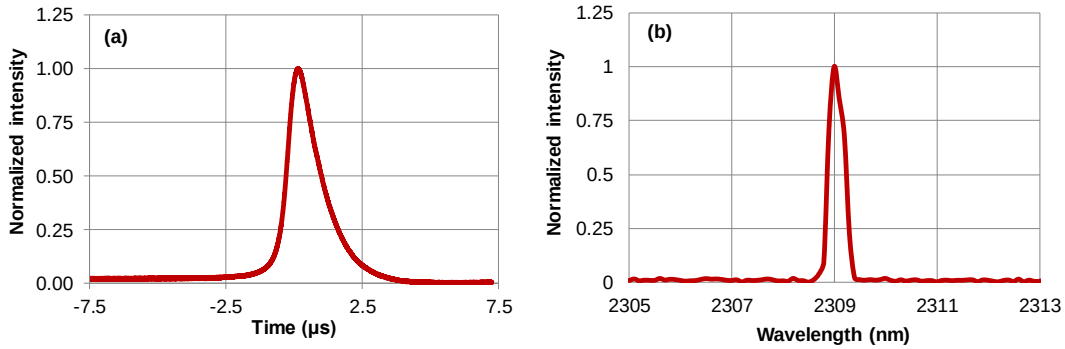


*Fig. 4.3 (a) Temporal pulse profile and (b) optical spectrum of the passively Q-switched $Tm^{3+}$:YLF laser.*

In Fig. 4.4, four different graphs show the variation of pulse duration, repetition rate, pulse energy, and peak power for different levels of pumping for the passively Q-switched $Tm^{3+}$:YLF laser. The pulse widths of the Q-switched laser displayed in Fig. 4.4(a) were between 1.2 and 1.4 µs. The measured repetition frequency of the output pulse was in the range of 300 Hz-2.1 kHz for double-pumped and 360 Hz-1.5 kHz for single-pumped laser cavity (Fig. 4.4 (b)). Figure 4.4 (b) shows the variation of the output pulse energy ($E_p$) (determined from $E_p = P_{out}/f_{rep}$, where $P_{out}$ = output power, $f_{rep}$ = repetition rate) as a function of the input pump power. In particular, at the maximum pump power of 890 mW, the pulse energy was 13 µJ for double pumping and 7 µJ for single pumping. The maximum peak power achieved ($P_{peak} = E_p/\tau_p$, $\tau_p$ = pulse width) was 10W in the passively Q-switched operation regime (Fig. 4.4(d)).

Based on the analysis of passive Q switching [113-115], the repetition frequency ($f_{rep}$) of the laser can be determined in terms of the round-trip small-signal gain ($G_0$) of the laser and round-trip small-signal loss ($Q_0$) of the saturable absorber as

$$f_{rep} = \frac{1}{\tau_f}\frac{G_0}{2Q_0}, \qquad (1)$$

where, $\tau_f$ is the fluorescence lifetime of the laser gain medium. The small-signal loss ($Q_0$) of the $Cr^{2+}$:ZnSe was determined from Eq. (1) by using the measured variation of the repetition frequency as a function of the input pump power.

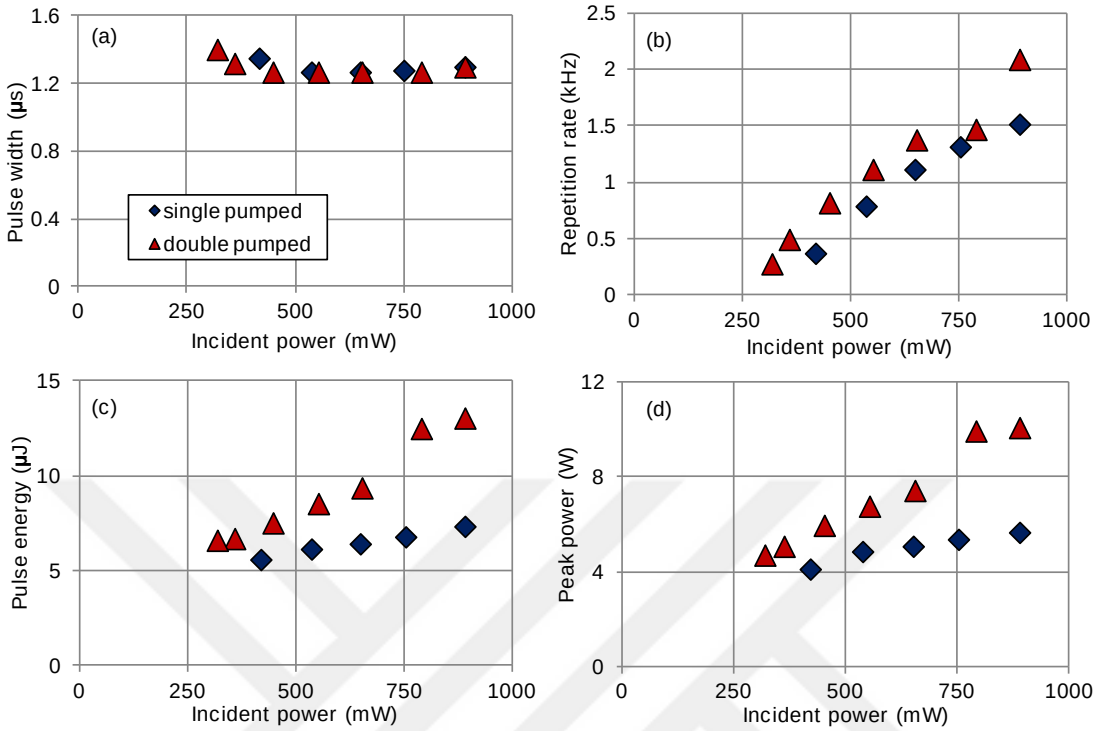


*Figure 4.4 The variation of the (a) pulse width, (b) repetition rate, (c) pulse energy, and (d) peak power as a function the incident pump power for the $Tm^{3+}$:YLF laser passively Q-switched with a $Cr^{2+}$:ZnSe saturable absorber.*

In order to calculate the small-signal gain ($G_0$) in Eq. (1), the average output power data ($P_{out}$) can be used for each pump power level, as described in Ref. [111] :

$$P_{out} = T\frac{P_{sat}}{2}\left(\frac{G_0}{G_{th}} - 1\right). \tag{2}$$

Here, $T$ is the transmission of the output coupler, $P_{sat}$ is the saturation power, $G_{th}$ is the round-trip threshold gain ($G_{th} = (L_c + T)$, $L_c$ = round-trip cavity loss). Furthermore, the saturation power ($P_{sat}$) is given by

$$P_{sat} = \frac{h\nu_L}{\sigma_e \tau_f} A, \tag{3}$$

where $h\nu_L$ is the photon energy at the lasing wavelength (0.54 eV), $\sigma_e$ is the emission cross section ($0.87\times10^{-21}\,cm^2$ [30]), and $\tau_f$ is the fluorescence lifetime (930 μs [61]). Also, $A$ is the effective cross-sectional area of the beam which can be estimated from $A = \pi\omega_{rms}^2$

, where $\omega_{rms}$ is the root-mean-squared value of the spot size. $\omega_{rms}$ was estimated as 39 μm from the ABCD analysis of the cavity near the center of the stability range. This resulted in a saturation power ($P_{sat}$) of 1.02 W. The round-trip loss of the cavity containing the $Cr^{2+}$:ZnSe saturable absorber was estimated from the threshold power analysis as 2.9% and this resulted in a threshold round-trip gain ($G_{th}$) of 3.9 %. The small-signal gain ($G_0$) was then determined for each value of the pump power by using the measured output power data (Fig. 2(b)) and Eq.s (2) and (3). Figure 4.5 shows the measured and fit variation of the small signal gain ($G_0$) as a function of $2\times f_{rep}\times\tau_f$ for single- and double- pumped cavities. From the least-squares best fit to the data, the small-signal loss ($Q_0$) estimated for the single and double pumping cases was (3.2 ± 0.4) % and (5.8 ± 1.8) %, with an average of (4.5 ± 0.4) %.

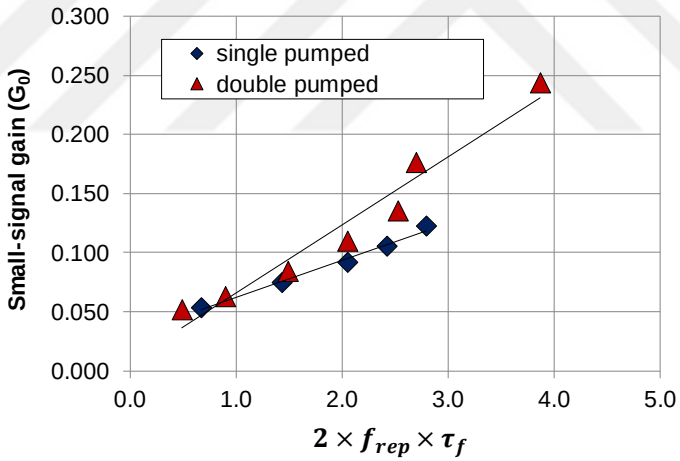


*Figure 4.5 Measured and fit variation of the small-signal gain ($G_0$) as a function of $2\times f_{rep}\times\tau_f$ for single and double pumping cases.*

### 4.4 Conclusions

In conclusion, we demonstrated, for the first time, the passively Q-switched of a 2.3-μm $Tm^{3+}$:YLF laser by inserting a $Cr^{2+}$:ZnSe saturable absorber into the resonator. Repetitive Q-switching of the $Tm^{3+}$:YLF laser could be achieved at all pump power levels above lasing threshold. The pulse widths were in the range of 1.2-1.4 μs and the repetition rates were in the range of 300Hz- 2.1kHz. The central wavelength of the optical spectrum was measured

to be at 2309 nm. For the passive Q-switching analysis, the pump power dependent repetition rates were further analyzed to estimate the small-signal loss of the $Cr^{2+}$:ZnSe absorber.

# Chapter 5

## Preliminary results on further pulsed operation of 2.3-μm $Tm^{3+}$:YLF laser

In this chapter, we will describe the preliminary results on pulsed operation of $Tm^{3+}$:YLF laser at 2.3 μm by using a semiconductor saturable absorber (SESAM) and a graphene saturable absorber. First, we will explain the preliminary results of Q-switching and mode locking of the 2.3-μm $Tm^{3+}$:YLF laser by using a semiconductor saturable absorber mirror (SESAM). Furthermore, we will describe the preliminary results on the graphene mode-locked $Tm^{3+}$:YLF laser at 2.3 μm.

### 5.1 SESAM-based pulsing experiments and preliminary results

Figure 5.1 shows the design of the commercial SESAM (SAM-2400-1-12.7g-500fs, BATOP GmBH) used for the passive Q-switching and mode locking of $Tm^{3+}$:YLF laser. The laser beam passes through an AR coating designed for 2.4 μm, a 620-μm-thick GaAs wafer, a saturable absorber layer, and reflects back from the 2.4-μm mirror coating. The reflectivity of the dielectric back mirror is reported to be above 98 % from 2300 nm to 2650 nm. The specifications of the SESAM given as follows: absorbance of 1%, the modulation depth of 0.6%, non-saturable loss of 0.4%, saturation fluence of 90 $\mu J/cm^2$, and relaxation time constant of 500 fs.

Figure 5.2 shows the experimental setup of the 2.3-μm $Tm^{3+}$:YLF laser Q-switched by using a commercial semiconductor saturable absorber mirror (SESAM). We used the same prism-tuned $Ti^{3+}$:sapphire laser described in continuous-wave and passive Q-switching experiments in Chapters 3 and 4. The output of the $Ti^{3+}$:sapphire laser was sent into the Brewster-cut $Tm^{3+}$:YLF gain medium by passing through a converging lens (L1) with a focal length of 75 mm, and input curved mirror (M3) with a radius of curvature (R) of 100 mm. The 9-mm-long, 1.5 at. % thulium-doped gain medium absorbed 78 %

of the 780-nm pump beam. The transmitted pump beam was retroreflected inside the crystal by using a curved mirror (M5, the radius of curvature R=75 mm) to increase the pumping efficiency via double pumping. The $Tm^{3+}$:YLF laser resonator consisted of five mirrors: three curved mirrors (M3-M4, with a radius of curvature R=100 mm and M6 with R=50mm), a flat SESAM high reflector and an output coupler with 1% transmission. The intracavity circulating laser beam was focused on the SESAM by using the 5-cm curved mirror (M6) on the high reflector arm. The SESAM used in the experiments was a commercial one which consisted of a highly reflecting coating at the center wavelength of 2400 nm. A 1.5-mm quartz birefringent tuning plate (BTP) was placed in the cavity for tuning the laser output to a wavelength, where the round-trip loss of the cavity would be minimum. The tuning range was in two distinct regions: between 2300-2325 nm and 2408-2423 nm. The laser output power was 5 mW and 7 mW when passively Q-switched at 2413 nm and 2307 nm, respectively. At the maximum output power of 20 mW at 2307 nm, the laser operated in pure cw regime. All the output powers were measured in the double pumping configuration.

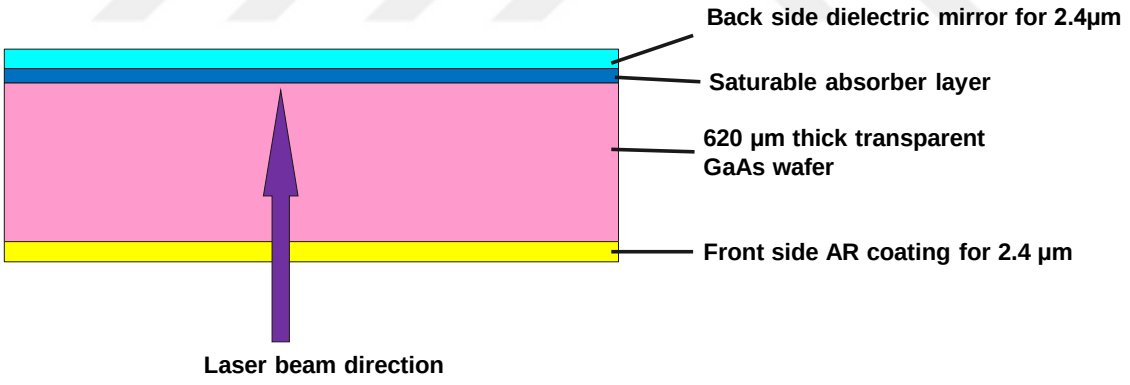


*Fig. 5.1 Schematic of the commercial SESAM used in the passive Q-switching and mode locking experiments of $Tm^{3+}$:YLF laser.*

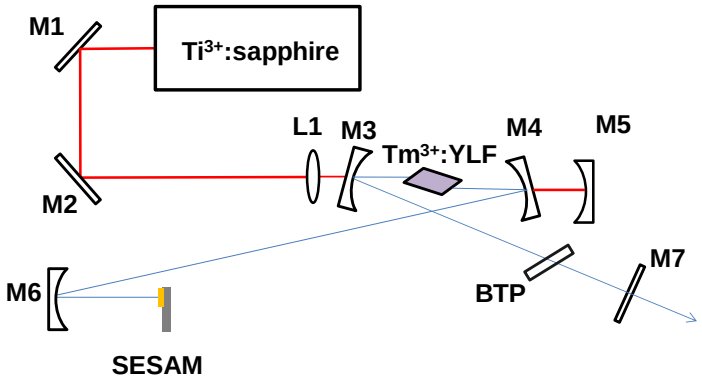


*Fig. 5.2 Schematic of the 2.3-µm $Tm^{3+}$:YLF laser passively Q-switched by using a semiconductor saturable absorber mirror (SESAM).*

The stable Q-switched output pulse train is shown in Fig. 5.3, where the repetition rate and pulse width were 1.9 kHz and 40 µs, respectively. In our laser tuning experiments, we observed pulses in the 1kHz-3.5kHz range at 2.4-µm and in the 2.7 kHz-6 kHz range at 2.3 µm.

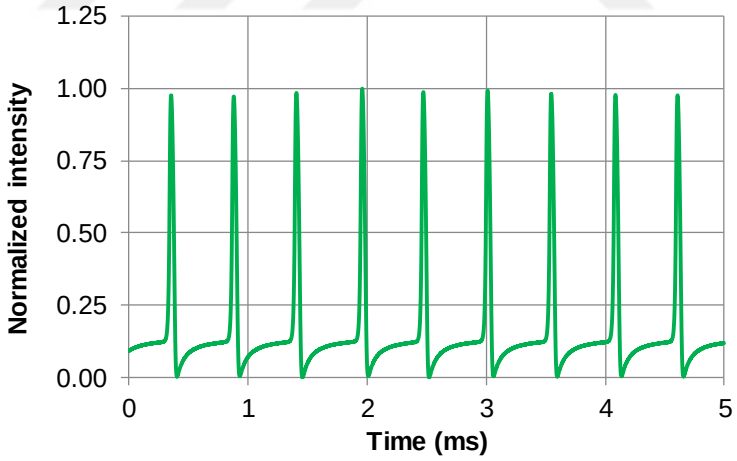


*Fig. 5.3 Measured pulse train of the Q-switched 2.3-µm $Tm^{3+}$:YLF laser, passively Q-switched with a SESAM.*

Figure 5.4 shows the experimental setup used in mode locking experiments performed with the SESAM. The pumping configuration and the cavity curved mirrors were the

same as in the experimental setup described in Fig. 5.2. These parts of the setup are not explained here to avoid redundancy. In order to initiate mode locking, we extended the cavity length of the experimental setup by about two meters, by adding a flat high reflector (M6) and a curved (M7, ROC=1000mm) high reflector in the high reflector arm by maintaining the q-preserving characteristic of the extension (Fig.5.3). In the final setup, the cavity length was about 3.5 meters. The pumping configuration was the same as in the experimental setup depicted in Fig. 5.2. In order to manage the intracavity group delay dispersion, a 6-mm, undoped YAG crystal was inserted at Brewster's angle in the output coupler arm. By using the described cavity, 21 mW (31 mW) of output power was obtained by single (double) pumping with 880 mW at 780 nm.

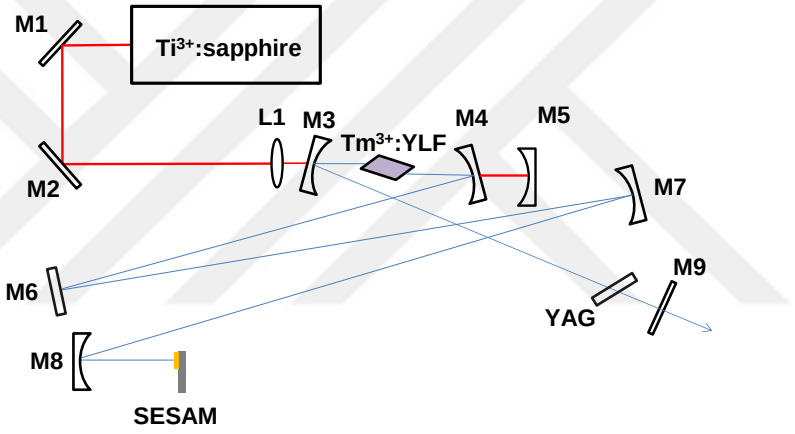


*Fig. 5.4 Experimental setup of the 2.3-µm $Tm^{3+}$:YLF laser mode-locked by using a SESAM.*

Figures 5.5 (a) and (b) show the measured pulse train, where the repetition rate of 42.4 MHz was well-matched with the repetition frequency of 42.6 MHz estimated from the cavity length (3.52 m). Figure 5.5 (b) shows that the laser could be operated in continuous-wave mode-locked regime.

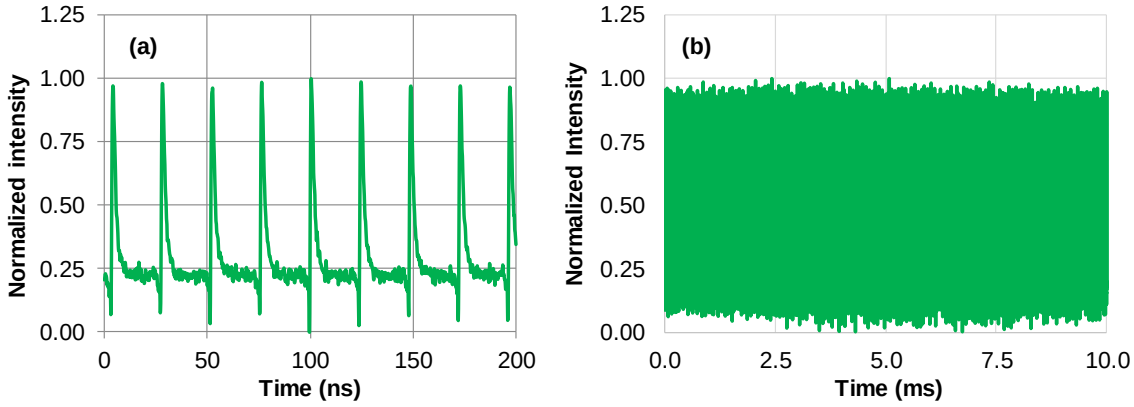


*Fig. 5.5 The recorded pulse train of the SESAM mode-locked 2.3-µm $Tm^{3+}$:YLF laser in (a) nanosecond, and (b) millisecond time scales.*

Furthermore, Fig. 5.6 shows that the fundamental tone of the generated pulse train was 52 dB above the noise floor at the fundamental beat note of 42.4 MHz, by using a radio frequency (RF) spectrum analyzer at the resolution bandwidth of 1 kHz. In our experiments, we did not observe any broadening of the optical spectrum measured with the scanning spectrometer having a resolution of 0.5 nm.

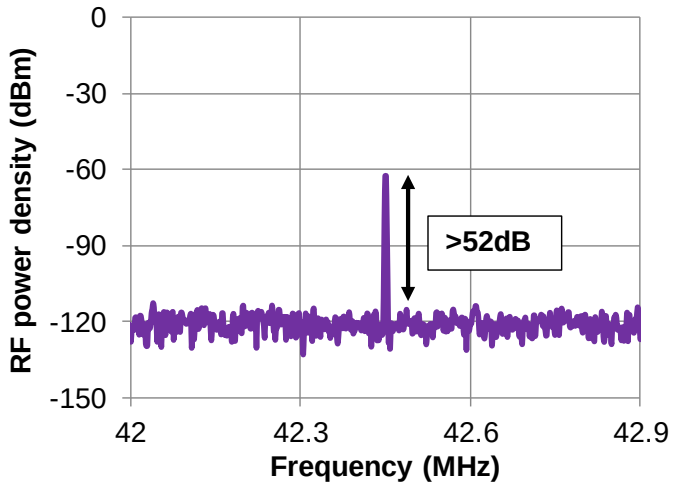


*Fig. 5.6 RF spectrum of the pulses generated with SESAM mode-locked 2.3-µm $Tm^{3+}$:YLF laser.*

## 5.2 Graphene saturable absorber based preliminary mode locking results

We used a graphene saturable absorber (GSA) transferred onto a 2-mm-thick $CaF_2$ substrate in our mode locking experiments. For this experiment, the same double pumping scheme as in the previous setup was used. We will describe only the high reflector arm to avoid redundancy. Two curved high reflectors (M6-M7, the radius of curvature R=50 mm) generated an additional focus where the graphene saturable absorber was inserted at Brewster's incidence. The Raman spectrum of the GSA given in Ref. [116], suggested that the transferred graphene was nearly a monolayer. The mirror used as the output coupler (OC) was designed as a highly reflecting mirror centered at 2450 nm and transmitted only 0.38% of the laser wavelength at 2305 nm. The laser output power was around 10 mW, when double-pumped with nearly 900 mW of pump power at 780 nm.

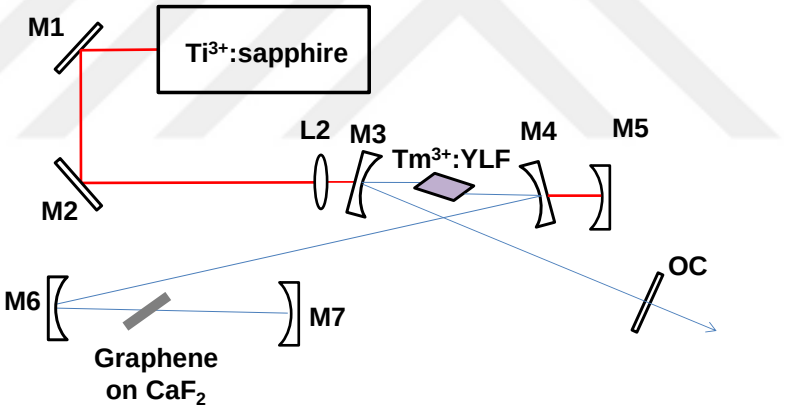


*Fig. 5.7 The experimental setup of the graphene mode-locked 2.3-µm $Tm^{3+}$:YLF laser.*

Figure 5.7 shows the measured optical spectrum of the 2.3-µm $Tm^{3+}$:YLF laser mode-locked by using the graphene saturable absorber. The full width at half maximum of the optical spectrum was measured as 1.9 nm by using a spectrometer with a resolution of 0.5 nm. This linewidth suggests 3-ps pulses if a $sech^2$ pulse profile is assumed.

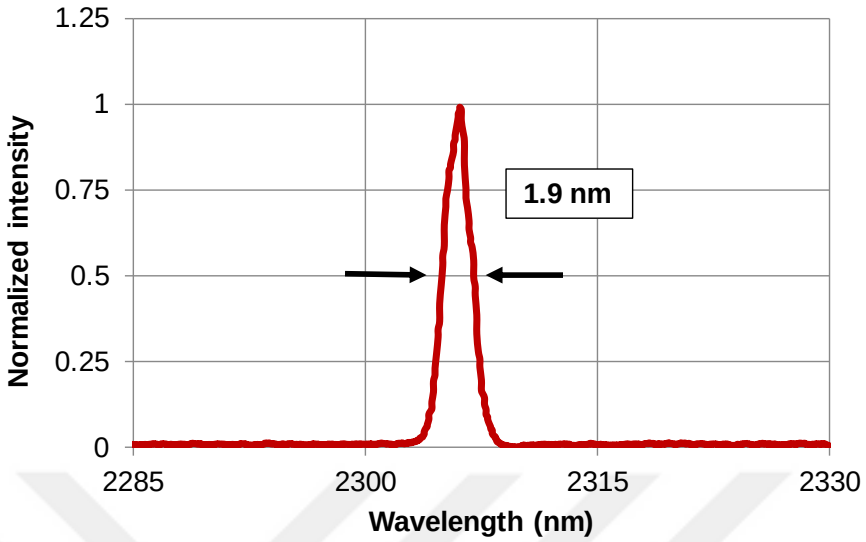


*Fig. 5.8 Optical output spectrum of the graphene mode-locked $Tm^{3+}$:YLF laser operating at 2.3 µm.*

The RF pulse spectrum can be seen in Fig. 5.9, where the fundamental beat note at 103.9 MHz was more than 57 dB above the noise floor. The RF spectrum was taken by using an RF spectrometer at 1 kHz resolution bandwidth.

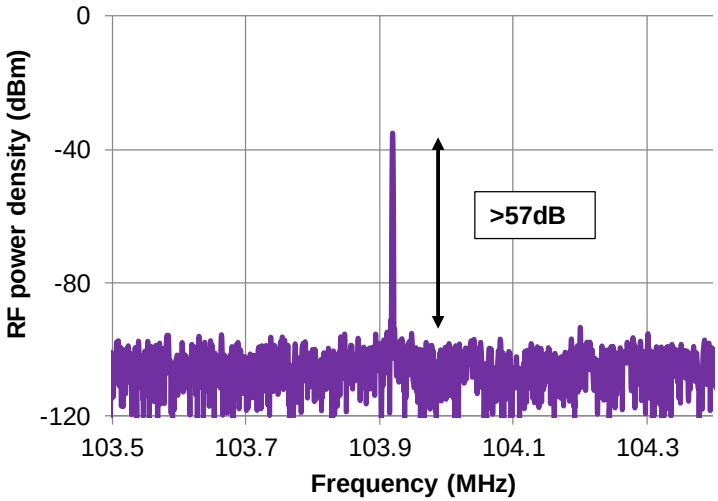


*Fig. 5.9 The RF pulse spectrum of the 2.3-µm $Tm^{3+}$:YLF laser mode-locked by using a monolayer graphene saturable absorber.*

## 5.3 Conclusions

In this chapter, we demonstrated preliminary data on Q-switched and mode-locked operation of the $Tm^{3+}$:YLF laser near 2.3 μm by using a SESAM and a graphene saturable absorber. The preliminary mode locking data require further optimization as well as pulse width measurements by using an intensity or interferometric autocorrelator. Furthermore, by careful dispersion management of the cavity, it should be possible to generate broader mode-locked optical spectra with shorter pulse durations. To date, there are only three recent pulsing results in the literature for the $Tm^{3+}$:YLF lasers operating at 2.3 μm, to the best of our knowledge: the passive Q-switched laser described in Chapter 4 [28], SESAM mode-locked laser with 94-ps pulses [73], and Kerr-lens mode locked resonator which produced 514-fs pulses [74]. Therefore, the additional methods described in this chapter for generating pulses with 2.3-μm $Tm^{3+}$:YLF laser suggest that other passive Q-switching and mode-locking methods can be applied to generate short pulses. The displayed preliminary results have the potential to be developed further in future studies.

# Chapter 6

## Conclusions

In this thesis, the continuous-wave diode pumping and pulsed operation of Alexandrite lasers at 760 nm and $Tm^{3+}$:YLF lasers at 2.3 μm were investigated. In Chapter 1, a concise description of the spectroscopic properties of transition metal and rare-earth doped laser crystals was presented. In particular, the energy level diagrams of the Alexandrite and $Tm^{3+}$:YLF crystals were described along with the laser literature involving these crystals and their lasing characteristics.

In Chapter 2, we described a single-mode diode-pumped and efficient Alexandrite laser operating at 760 nm. First, the temperature-dependent emission intensity and fluorescence lifetime of the Alexandrite crystal were experimentally shown to decrease as a function of the crystal temperature. In the continuous-wave laser experiments, the maximum laser output power and the highest slope efficiency obtained were 48 mW and 36 %, respectively. The corresponding output coupler transmission and the maximum pump power were 0.5% and 170 mW, respectively. The diode-pumped Alexandrite laser was broadly tunable from 736 nm to 823 nm. In the previous studies, laser tuning was obtained at wavelengths as short as 701 nm with a pulsed Alexandrite laser [38]. Moreover, as the crystal temperature increased from 25 °C to 200 °C, the center wavelength of the laser shifted from 760 nm to 805 nm. In the temperature-dependent lasing experiments, the slope efficiency of the Alexandrite laser dropped from 36% to 12% at 0.5% output coupler transmission, when the temperature of the gain medium increased from 25 °C to 200 °C. The self Q-switched (SQS) operation was observed by slightly changing the curved mirror separation or by changing the alignment of the cavity. The generated self-Q-switched pulses attained repetition rates in the range of 10-35 kHz and pulsewidths in the range of 5-15 μs. The results obtained with this laser offered a

low-cost and efficient way to reach around 800 nm, and it has the potential to be an attractive source for many applications, especially in medicine.

The second part of this thesis focused on the diode pumping of continuous-wave $Tm^{3+}$:YLF lasers described in Chapter3. A thorough investigation of the continuous-wave laser characteristics of the $Tm^{3+}$:YLF laser was provided. First, by using a narrow-line, tunable $Ti^{3+}$:sapphire pump laser, the excitation spectrum of the $Tm^{3+}$:YLF crystal was measured. This way, the efficient pumping lines around 780 nm were determined in detail for diode-pumping. Second, the pump absorption saturation behavior of the 1.5 at. % $Tm^{3+}$:YLF gain medium was investigated by tuning the $Ti^{3+}$:sapphire wavelength to 792 nm. The absorption cross section was determined by using the power-dependent and position-dependent absorption saturation data. The average absorption cross section value was determined to be $\sigma_a = 0.77 \times 10^{-20} cm^2$. In addition, the continuous-wave and low-threshold operation of the 2.3-μm $Tm^{3+}$:YLF laser was studied by using a low-cost, single-mode, 120-mW pump diode operating at 792 nm. The threshold pump power of this laser was 25 mW at the output coupler transmission of 1%. The maximum output power of 10.5 mW was obtained with 11.4% slope efficiency and 119 mW of pump power. The variation of the laser output power, slope efficiency and threshold pump power was investigated by using a 250-mW diode-pumped laser cavity with variable output coupling. In these measurements, the highest measured slope efficiency was about 10% at 0.7% transmission of the effective output coupler. Beyond this transmission value, the slope efficiencies decreased possibly due to a nonradiative upconversion process. From the best fit values of the measured threshold pump powers, the stimulated emission cross section for the gain medium was determined to be $\sigma_e = (0.55 \pm 0.04) \times 10^{-20} cm^2$. This laser was one of the first diode-pumped, 2.3-μm $Tm^{3+}$:YLF lasers. Another study that demonstrated the 2.3-μm operation of $Yb^{3+}$:$Tm^{3+}$:YLF employed a 5-W 685 nm diode, and a 20-W 960 nm laser diode [72]. The threshold pump power for the $Yb^{3+}$ co-doped $Tm^{3+}$:YLF laser was about 2.6 W at 1.2% output coupling. Also, it generated the highest output power of 620 mW at 2.3 μm from a $Tm^{3+}$:YLF laser. The diode-pumped laser that

was demonstrated in this thesis offers a simple and efficient way to reach the 2.3 μm wavelength by using only one 120-mW pump diode operating at 792 nm and without the need for co-pumping with two different pump lasers.

Following the investigation of the continuous-wave characteristics, the passively Q-switched operation of the 2.3-μm $Tm^{3+}$:YLF laser was investigated in Chapter 4. To the best of our knowledge, this was the first demonstration of pulsed operation of $Tm^{3+}$:YLF lasers at 2.3 μm by using a $Cr^{2+}$:ZnSe saturable absorber [28]. The passively Q-switched operation was obtained at all pump power levels above the lasing threshold. The pulse widths of the repetitive pulses were in the range of 1.2-1.4 μs with repetition rates between 0.3 and 2.1 kHz. From the measured variation of repetition rates as a function of the incident pump power, the average small-signal loss of the $Cr^{2+}$:ZnSe saturable absorber was estimated to be 4.5 %. The pulse energy of 13 μJ (7 μJ) was obtained with double (single) pumping at the highest pump power of 890 mW. The maximum peak power obtained for the double pumping case was 10 W. The thulium-based pulsed laser operation in the mid-infrared explained in this thesis has drawn much interest. Soon after the Q-swiched operation described in this thesis [28], 94-ps pulses were generated by using a semiconductor saturable absorber mirror (SESAM) [73], and 514-fs pulses were generated by Kerr-lens mode locking [74].

In Chapter 5, preliminary experimental data were presented about the pulsed operation of 2.3-μm $Tm^{3+}$:YLF lasers by using saturable absorbers other than $Cr^{2+}$:ZnSe. First, by using a commercial semiconductor saturable absorber mirror (SESAM), Q-switched pulses with repetition rates of 1 kHz-6 kHz were obtained. Furthermore, by extending the cavity length, we obtained 42.4 MHz pulse repetition rates, which was well-matching the estimated pulse repetition frequency of the 3.52-m-long cavity for mode locking. We further recorded the preliminary mode-locking data of the cavity containing a graphene saturable absorber. We used a monolayer graphene saturable absorber on a $CaF_2$ substrate. By using this scheme, a mode-locked optical spectrum with a bandwidth of 1.9 nm and an RF signal of more than 57 dB above the noise floor were recorded. The preliminary data obtained with different saturable absorbers suggest that it is possible to

generate mode-locked or Q-switched pulses at 2.3-μm by using various saturable absorbers. For the graphene mode locking case, the 1.9 nm of broadening that was observed in the optical spectrum can in principle be increased by a careful management of the cavity dispersion. This way, it should be possible to generate shorter pulses allowed by the gain bandwidth of the $Tm^{3+}$:YLF crystal at 2.3 μm.

This thesis made many primary contributions to the solid-state lasers research. First, the demonstration of low threshold, diode-pumped and continuous-wave operation of Alexandrite lasers at 760 nm and $Tm^{3+}$:YLF lasers at 2305 nm were achieved. There are many potential improvements that can be made to contribute to these lasers. Alexandrite has a broad gain bandwidth which can support the generation of sub-10-fs pulses. To date, there is only one study that reports the mode-locked operation of the Alexandrite lasers with 170-fs pulses [60]. Shorter pulse generation with the Alexandrite lasers can significantly increase the achievable peak powers and the pulse energies around 760 nm center wavelength. By a careful dispersion management in the mode-locked Alexandrite cavities, generation of shorter pulses is possible.

Although 2.3-μm laser emission of the thulium-doped gain media is well known, the pulsed operation regimes are recently investigated in the literature, as discussed above. Increasing the variety of the techniques and saturable absorbers used for mode-locked operation is quite important to have a robust laser source generate a line of lasers used in various applications. To date, the duration of the shortest pulses generated from a 2.3-μm $Tm^{3+}$:YLF laser is 514 fs [74]. It is also possible to generate sub-50-fs second pulses if all the available tuning range is locked. In Chapter 5, we have demonstrated preliminary data of the mode-locked cavities by using a semiconductor saturable absorber mirror and a graphene saturable absorber. By careful management of the group delay dispersion (GDD) of the laser cavity, it is possible to generate shorter pulses. However, we note here that, it can be challenging to compensate the excessive dispersion of a 9-mm-long YLF crystal (GDD=-1377$fs^2$ per round trip at 2.3 μm [74]) due to to the relatively low nonlinear refractive index of the YLF crystal ($n_2$=1.72×$10^{-20}$ $m^2$/W [117]). One can adress this issue by increasing the effective Kerr nonlinearity or by increasing the length of the

of the laser cavity to provide higher pulse energies. Furthermore, the efficient pumping of the ZGP optical parametric oscillators described in Chapter 1 could be achieved by using $Tm^{3+}$:YLF lasers operating at 2.3-μm. In addition, the pumping line at 685 nm could be used for both continuous-wave and pulsed operations of $Tm^{3+}$:YLF lasers. The absorption coefficient at 685 nm is three times larger than that of at 780 nm [61]. Therefore, by using the excitation line at 685 nm, a lower concentration of $Tm^{3+}$ could be used which will potentially diminish the unwanted effect of the decreasing slope efficiencies at higher output couplings described in Chapter 3. As we have described in Chapter 3, the output wavelength of the single-mode diodes could be tuned to higher wavelengths if a diode laser could not be obtained at the center wavelength of 685 nm. In chapter 3, we tuned the room temperature output wavelength of the laser diode from 785 nm to 792 nm for the efficient pumping of the $Tm^{3+}$:YLF crystal. One can also use the same method for efficient excitation without decreasing pump beam quality.

As the technology of pulsed and continous-wave 2.3-μm $Tm^{3+}$:YLF lasers is further developed, we expect that they will find numerous applications in medicine, spectroscopy and remote sensing.

## BIBLIOGRAPHY


1. A. Einstein, "On the Quantum Theory of Radiation," Physikalische Zeitschrift **18**, 121-128 (1917).
2. J. P. Gordon, H. J. Zeiger, and C. H. Townes, "The Maser-New Type of Microwave Amplifier, Frequency Standard, and Spectrometer," Physical Review **99**, 1264-1274 (1955).
3. T. H. Maiman, "Stimulated optical radiation in ruby," Nature **187**, 493-494 (1960).
4. A. Javan and J. W. R. Bennett, "Gas optical maser," (Google Patents, 1964).
5. E. Snitzer, "Optical Maser Action of $Nd^{+3}$ in A Barium Crown Glass," Physical Review Letters **7**, 444-446 (1961).
6. R. N. Hall, G. E. Fenner, J. Kingsley, T. Soltys, and R. Carlson, "Coherent light emission from GaAs junctions," Physical Review Letters **9**, 366 (1962).
7. P. P. Sorokin and J. Lankard, "Stimulated emission observed from an organic dye, chloro-aluminum phthalocyanine," IBM Journal of Research and Development **10**, 162-163 (1966).
8. H.-M. Tzeng, K. F. Wall, M. B. Long, and R. K. Chang, "Laser emission from individual droplets at wavelengths corresponding to morphology-dependent resonances," Opt. Lett. **9**, 499-501 (1984).
9. Y.-C. Chen, Q. Chen, and X. Fan, "Lasing in blood," Optica **3**, 809-815 (2016).
10. A. Jonáš, M. Aas, Y. Karadag, S. Manioğlu, S. Anand, D. McGloin, H. Bayraktar, and A. Kiraz, "In vitro and in vivo biolasing of fluorescent proteins suspended in liquid microdroplet cavities," Lab on a Chip **14**, 3093-3100 (2014).
11. "Apollo Lunar Surface Journal" (NASA, 18/09/2016), retrieved 03/10/17, https://www.hq.nasa.gov/alsj/a14/AS14-67-9386HR.jpg.
12. "McDonald Laser Ranging Station" (10/05/12), retrieved 03/10/17, http://www.csr.utexas.edu/mlrs/.
13. L. D. Smullin and G. Fiocco, "Optical echoes from the moon," Nature **194**, 1267-1267 (1962).
14. P. Bender, D. Currie, R. Dicke, D. Eckhardt, J. E. Faller, W. Kaula, J. Mulholland, H. Plotkin, S. Poultney, and E. Silverberg, "The lunar laser ranging experiment," Science **182**, 229-238 (1973).
15. Y. Liang, J. Huang, M. Ren, B. Feng, X. Chen, E. Wu, G. Wu, and H. Zeng, "1550-nm time-of-flight ranging system employing laser with multiple repetition rates for reducing the range ambiguity," Opt. Express **22**, 4662-4670 (2014).
16. S. Sakadzic, U. Demirbas, T. R. Mempel, A. Moore, S. Ruvinskaya, D. A. Boas, A. Sennaroglu, F. X. Kaertner, and J. G. Fujimoto, "Multi-photon microscopy with a low-cost and highly efficient Cr:LiCAF laser," Opt. Express **16**, 20848-20863 (2008).
17. K. A. Ghany and M. Newishy, "Cutting of 1.2 mm thick austenitic stainless steel sheet using pulsed and CW Nd: YAG laser," Journal of Materials Processing Technology **168**, 438-447 (2005).

18. M. Keskitalo, K. Mäntyjärvi, J. Sundqvist, J. Powell, and A. Kaplan, "Laser welding of duplex stainless steel with nitrogen as shielding gas," Journal of Materials Processing Technology **216**, 381-384 (2015).
19. W. E. Frazier, "Metal additive manufacturing: a review," Journal of Materials Engineering and Performance **23**, 1917-1928 (2014).
20. A. Extance, "Laser weapons get real," Nature **521**, 408 (2015).
21. R. Holzwarth, M. Zimmermann, T. Udem, and T. Hansch, "Optical clockworks and the measurement of laser frequencies with a mode-locked frequency comb," IEEE journal of quantum electronics **37**, 1493-1501 (2001).
22. A. E. H. P. A. Franken, C. W. Peters, and G. Weinreich, "Generation of Optical Harmonics," Physical Review Letters **7**, 118-119 (1961).
23. E. N. Leith and J. Upatnieks, "Reconstructed Wavefronts and Communication Theory*," J. Opt. Soc. Am. **52**, 1123-1130 (1962).
24. Y. N. Denisyuk, "On the reflection of optical properties of an object in a wave field of light scattered by it," Doklady Akademii Nauk SSSR **144**, 1275-1278 (1962).
25. "All Nobel Prizes in Physics" (Nobelprize.org), retrieved 3 Oct 2017, http://www.nobelprize.org/nobel_prizes/physics/laureates/index.html.
26. "All Nobel Prizes in Chemistry," (2014).
27. R. Schoenlein, L. Peteanu, R. Mathies, and C. Shank, "The first step in vision: femtosecond isomerization of rhodopsin," Science **254**, 412-416 (1991).
28. F. Canbaz, I. Yorulmaz, and A. Sennaroglu, "2.3-μm $Tm^{3+}$:YLF laser passively Q-switched with a $Cr^{2+}$:ZnSe saturable absorber," Opt. Lett. **42**, 1656-1659 (2017).
29. I. Yorulmaz, E. Beyatli, A. Kurt, A. Sennaroglu, and U. Demirbas, "Efficient and low-threshold Alexandrite laser pumped by a single-mode diode," Opt. Mater. Express **4**, 776-789 (2014).
30. V. Sudesh and J. A. Piper, "Spectroscopy, Modeling, and Laser Operation of Thulium Crystals at 2.3 μm," IEEE Journal of Quantum Electronics **QE-36**, 879-884 (2000).
31. I. F. Elder and M. J. P. Payne, "Lasing in diode-pumped Tm:YAP, Tm,Ho:YAP and Tm,Ho:YLF," Opt Commun **145**, 329-339 (1998).
32. O. Svelto, *Principles of Lasers* (Plenum Press, New York, 1989).
33. J. C. Walling, H. P. Jenssen, R. C. Morris, E. W. O'Dell, and O. G. Peterson, "Tunable-laser performance in BeAl2O:Cr3+," Opt. Lett. **4**(1979).
34. R. C. Morris and C. F. Cline, "Chromium Doped Beryllium Aluminate Lasers," (1976).
35. J. C. Walling, H. P. Jenssen, R. C. Morris, E. W. O'Dell, and O. G. Peterson, "Tunable laser performance in $BeAl_2O_4Cr^{3+}$," Opt. Lett. **4**, 182-183 (1979).
36. R. Scheps, B. M. Gately, J. F. Myers, J. S. Krasinski, and D. F. Heller, "Alexandrite laser pumped by semiconductor lasers," Applied Physics Letters **56**, 2288-2290 (1990).

37. G. V. Bukin, S. Y. Volkov, V. N. Matrosov, B. K. Sevast'yanov, and M. I. Timoshechkin, "Stimulated emission from alexandrite ($BeAl_2O_4$ :$Cr^{3+}$)," Soviet Journal of Quantum Electronics **8**, 671 (1978).
38. J. C. Walling, O. G. Peterson, H. P. Jenssen, R. C. Morris, and E. W. O`Dell, "Tunable alexandrite lasers," IEEE Journal of Quantum Electronics **16**, 1302-1315 (1980).
39. D. M. Winker, R. H. Couch, and M. McCormick, "An overview of LITE: NASA's lidar in-space technology experiment," Proceedings of the IEEE **84**, 164-180 (1996).
40. J. A. McKay and T. D. Wilkerson, "Laser source for space-flight elastic backscatter, differential absorption, and wind speed Doppler lidar," in *Optical Spectroscopic Techniques and Instrumentation for Atmospheric and Space Research II*, (International Society for Optics and Photonics, 1996), 19-32.
41. M. Strotkamp, U. Witte, A. Munk, A. Hartung, S. Gausmann, S. Hengesbach, M. Traub, H.-D. Hoffmann, J. Hoeffner, and B. Jungbluth, "Broadly tunable, longitudinally diode-pumped Alexandrite laser," in *Solid State Lasers XXIII: Technology and Devices*, (International Society for Optics and Photonics, 2014), 89591G.
42. P. F. Moulton, "An Investigation of the Co:$MgF_2$ Laser System," IEEE Journal of Quantum Electronics **21**, 1582-1595 (1985).
43. S. Ghanbari and A. Major, "High power continuous-wave Alexandrite laser with green pump," Laser Physics **26**, 075001 (2016).
44. J. W. Kuper, T. Chin, and H. E. Aschoff, "Extended Tuning Range of Alexandrite at Elevated Temperatures," in OSA Proceedings Series (Optical Society of America, 1990), CL3.
45. S. Guch and C. E. Jones, "Alexandrite-Laser Performance at High-Temperature," Optics Letters **7**, 608-610 (1982).
46. H. Samelson, J. C. Walling, and D. F. Heller, "Unique Applications of Alexandrite Lasers," P Soc Photo-Opt Inst **335**, 85-94 (1982).
47. S. Liu, J. Liu, and L. Wang, "High output energy tunable alexandrite laser " Chinese Optics Letters **5**, 16-18 (2007).
48. P. Bakule, P. E. G. Baird, M. G. Boshier, S. L. Cornish, D. F. Heller, K. Jungmann, I. C. Lane, V. Meyer, P. H. G. Sandars, W. T. Toner, M. Towrie, and J. C. Walling, "A chirp-compensated, injection-seeded alexandrite laser," Appl Phys B-Lasers O **71**, 11-17 (2000).
49. K. Torizuka, M. Yamashita, and T. Yabiku, "Continuous-Wave Alexandrite Laser-Pumped by a Direct-Current Mercury Arc Lamp," Applied Optics **32**, 7394-7398 (1993).
50. J. Walling, O. Peterson, and R. Morris, "Tunable CW alexandrite laser," Quantum Electronics, IEEE Journal of **16**, 120-121 (1980).
51. M. J. Damzen, G. M. Thomas, and A. Minassian, "Multi-watt diode pumped Alexandrite laser operation," in *CLEO 2013*, 2013),

52. E. Beyatli, I. Baali, B. Sumpf, G. Erbert, A. Leitenstorfer, A. Sennaroglu, and U. Demirbas, "Tapered Diode Pumped Continuous Wave Alexandrite Laser " J Opt Soc Am B (2013).
53. X. Peng, A. Marrakchi, J. Walling, and D. F. Heller, "Watt-level red and UV output from a CW diode array pumped tunable alexandrite laser," in *Lasers and Electro-Optics, 2005. (CLEO). Conference on*, 2005), 479-481 Vol. 471.
54. R. Scheps, J. F. Myers, T. R. Glesne, and H. B. Serreze, "Monochromatic End-Pumped Operation Of An Alexandrite Laser," Opt Commun **97**, 363-366 (1993).
55. M. Strotkamp, U. Witte, A. Munk, A. Hartung, S. Gausmann, S. Hengesbach, M. Traub, J. Hoeffner, and B. Jungbluth, "Broadly tunable, diode pumped Alexandrite laser," in *Advanced Solid State Lasers 2013,* (Paris, France 2013).
56. A. Teppitaksak, A. Minassian, G. M. Thomas, and M. J. Damzen, "High efficiency >26 W diode end-pumped Alexandrite laser," Opt. Express **22**, 16386-16392 (2014).
57. P. Pichon, A. Barbet, J.-P. Blanchot, F. Druon, F. Balembois, and P. Georges, "LED-pumped alexandrite laser oscillator and amplifier," Opt. Lett. **42**, 4191-4194 (2017).
58. U. Parali, X. Sheng, A. Minassian, G. Tawy, J. Sathian, G. M. Thomas, and M. J. Damzen, "Diode-pumped Alexandrite laser with passive SESAM Q-switching and wavelength tunability," Opt Commun (2017).
59. A. Hariharan, J. Squier, M. Fermann, M. Stock, and D. Harter, "Alexandrite-pumped alexandrite regenerative amplifier for femtosecond pulse amplification," Opt. Lett. **21**, 128-130 (1996).
60. S. Ghanbari, R. Akbari, and A. Major, "Femtosecond Kerr-lens mode-locked Alexandrite laser," Opt. Express **24**, 14836-14840 (2016).
61. J. F. Pinto and L. Esterowitz, "$Tm^{3+}$:YLF laser continuously tunable between 2.20 and 2.46 μm," Opt. Lett. **19**, 883-885 (1994).
62. E. Beyatlı, S. Naghizadeh, A. Kurt, and A. Sennaroglu, "Low-cost low-threshold diode end-pumped Tm:YAG laser at 2.016 μm," Applied Physics B **109**, 221-225 (2012).
63. C. E. Aleshire, C. X. Yu, P. A. Reed, and T. Y. Fan, "Efficient cryogenic near-infrared Tm:YLF laser," Opt. Express **25**, 13408-13413 (2017).
64. C. R. Pollock, F. R. Petersen, D. A. Jennings, J. S. Wells, and A. G. Maki, "Absolute Frequency Measurements of the 2-0-Band of CO at 2.3 μm; Calibration Standard Frequencies from High-Resolution Color Center Laser Spectroscopy," J Mol Spectrosc **99**, 357-368 (1983).
65. F. J. McAleavey, J. O'Gorman, J. F. Donegan, J. Hegarty, and G. Maze, "Extremely high sensitivity gas detection at 2.3 μm using a grazing incidence $Tm^{3+}$ fibre laser cavity," Sensors and Actuators a-Physical **87**, 107-112 (2001).
66. J. Cihelka, I. Matulkova, and S. Civis, "Laser diode photoacoustic and FTIR laser spectroscopy of formaldehyde in the 2.3 μm and 3.5 μm spectral range," J Mol Spectrosc **256**, 68-74 (2009).

67. R. J. Wang, S. Sprengel, G. Boehm, M. Muneeb, R. Baets, M. C. Amann, and G. Roelkens, "2.3 μm range InP-based type-II quantum well Fabry-Perot lasers heterogeneously integrated on a silicon photonic integrated circuit," Opt. Express **24**, 21081-21089 (2016).
68. J. T. Olesberg, M. A. Arnold, C. Mermelstein, J. Schmitz, and J. Wagner, "Tunable laser diode system for noninvasive blood glucose measurements," Appl. Spectrosc. **59**, 1480-1484 (2005).
69. S. T. Fard, W. Hofmann, P. T. Fard, G. Bohm, M. Ortsiefer, E. Kwok, M. C. Amann, and L. Chrostowski, "Optical absorption glucose measurements using 2.3-μm vertical-cavity semiconductor lasers," IEEE Photonics Technol. Lett. **20**, 930-932 (2008).
70. R. K. Feaver, R. D. Peterson, and P. E. Powers, "Longwave-IR optical parametric oscillator in orientation-patterned GaAs pumped by a 2 μm Tm,Ho:YLF laser," Opt. Express **21**, 16104-16110 (2013).
71. P. A. Budni, C. R. Ibach, S. D. Setzler, E. J. Gustafson, R. T. Castro, and E. P. Chicklis, "50-mJ, Q-switched, 2.09-μm holmium laser resonantly pumped by a diode-pumped 1.9-mu m thulium laser," Opt. Lett. **28**, 1016-1018 (2003).
72. P. S. De Matos, N. U. Wetter, L. Gomes, I. M. Ranieri, and S. L. Baldochi, "A high power 2.3 μm Yb:Tm:YLF laser diode-pumped simultaneously at 685 and 960 nm," J. Opt. A: Pure Appl. Opt. **10**, 104009 (2008).
73. R. Soulard, A. Tyazhev, J.-L. Doualan, A. Braud, A. Hideur, M. Laroche, B. Xu, and P. Camy, "2.3 μm $Tm^{3+}$:YLF mode-locked laser," Opt. Lett. **42**, 3534-3536 (2017).
74. F. Canbaz, I. Yorulmaz, and A. Sennaroglu, "Kerr-lens mode-locked 2.3-μm $Tm^{3+}$:YLF laser as a source of femtosecond pulses in the mid-infrared," Opt. Lett. **42**, 3964-3967 (2017).
75. E. Sorokin, "Solid-state materials for few-cycle pulse generation and amplification," in *Few-cycle laser pulse generation and its applications*, F. X. Kartner, ed. (Springer-Verlag, Berlin, 2004), pp. 3-71.
76. J. C. Walling, D. F. Heller, H. Samelson, D. J. Harter, J. A. Pete, and R. C. Morris, "Tunable Alexandrite Lasers - Development and Performance," IEEE Journal of Quantum Electronics **21**, 1568-1581 (1985).
77. V. V. Fedorov, S. B. Mirov, A. Gallian, D. V. Badikov, M. P. Frolov, Y. V. Korostelin, V. I. Kozlovsky, A. I. Landman, Y. P. Podmar'kov, V. A. Akimov, and A. A. Voronov, "3-77-5.05-μm tunable solid-state lasers based on $Fe^{2+}$-doped znse crystals operating at low and room temperatures," IEE Journal of Quantum Electronics **42**, 907-917 (2006).
78. M. Stalder, M. Bass, and B. H. T. Chai, "Thermal quencing of fluoresence in chromium-doped fluoride laser crystals," Journal of Optical Society of America B **9**, 2271-2273 (1992).
79. M. L. Shand and H. P. Jenssen, "Temperature-Dependence of the Excited-State Absorption of Alexandrite," IEEE J. Quantum Electron. **19**, 480-484 (1983).

80. J. W. Kuper, T. Chin, and H. E. Aschoff, "Extended tuning of Alexandrite laser at elevated temperetures," in *Advanced Solid State Lasers*, (OSA, Salt Lake City, Utah, 1990).
81. R. C. Powell, L. Xi, X. Gang, G. J. Quarles, and J. C. Walling, "Spectroscopic Properties of Alexandrite Crystals," Phys. Rev. B **32**, 2788-2797 (1985).
82. A. B. Suchocki, G. D. Gilliland, R. C. Powell, J. M. Bowen, and J. C. Walling, "Spectroscopic Properties of Alexandrite Crystals .2.," J. Lumin. **37**, 29-37 (1987).
83. E. Beyatli, I. Baali, B. Sumpf, G. Erbert, A. Leitenstorfer, A. Sennaroglu, and U. Demirbas, "Tapered diode-pumped continuous-wave alexandrite laser," J. Opt. Soc. Am. B **30**, 3184-3192 (2013).
84. P. Beaud, M. C. Richardson, Y. F. Chen, and B. H. T. Chai, "Optical Amplification Characteristics of Cr-LiSAF and Cr-LiCAF under Flashlamp-Pumping," IEEE J. Quantum Electron. **30**, 1259-1266 (1994).
85. V. Pilla, H. P. Jenssen, A. Cassanho, and T. Catunda, "Discrimination between thermal quenching of the fluorescence and Auger upconversion processes using thermal lens technique," Opt. Comm. **271**, 184-189 (2007).
86. J. A. Caird, L. G. DeShazer, and J. Nella, "Characteristics of room-temperature 2.3-μm laser emission from $Tm^{3+}$ in YAG and $YAlO_3$," IEEE J. Quantum Electron. **11**, 874-881 (1975).
87. D. Findlay and R. A. Clay, "The measurement of internal losses in 4-level lasers," Physics Letters **20**, 277-278 (1966).
88. S. A. Payne, L. L. Chase, H. W. Newkirk, L. K. Smith, and W. F. Krupke, "$LiCaAlF_6$:$Cr^{3+}$ a promising new solid-state laser material," IEEE J. Quantum Electron. **24**, 2243-2252 (1988).
89. J. C. Walling, O. G. Peterson, H. P. Jenssen, R. C. Morris, and E. W. Odell, "Tunable Alexandrite Lasers," IEEE Journal of Quantum Electronics **16**, 1302-1315 (1980).
90. M. L. Shand and J. C. Walling, "Excited-State Absorption in the Lasing Wavelength Region of Alexandrite," IEEE Journal of Quantum Electronics **18**, 1152-1155 (1982).
91. I. Freund, "Self-Q-Switching in Ruby Lasers," Applied Physics Letters **12**, 388-& (1968).
92. E. Beyatlı, A. Sennaroglu, and U. Demirbas, "Self-Q-Switched Cr:LiCAF Laser," Journal of Optical Society of America B **30**, 914-921 (2013).
93. M. Birnbaum and C. L. Fincher, "Self-Q-switched $Nd^{+3}$:YAG and ruby lasers," Proceedings of the IEEE **57**, 804-& (1969).
94. A. Szabo and L. E. Erickson, "Self-Q-Switching of Ruby Lasers at 77 Degrees K," IEEE Journal of Quantum Electronics **QE 4**, 692-& (1968).
95. B. C. Weber and A. Hirth, "Presentation of a new and simple technique of Q-switching with a $LiSrAlF^6$: $Cr^{3+}$ oscillator," Opt Commun **149**, 301-306 (1998).
96. S. T. Lai and M. L. Shand, "High-Efficiency Cw Laser-Pumped Tunable Alexandrite Laser," Journal of Applied Physics **54**, 5642-5644 (1983).

97. J. C. Walling, O. G. Peterson, and R. C. Morris, "Tunable Cw Alexandrite Laser," IEEE Journal of Quantum Electronics **16**, 120-121 (1980).
98. W. Gadomski and B. Ratajska-Gadomska, "Self-pulsations in phonon-assisted lasers," J Opt Soc Am B **15**, 2681-2688 (1998).
99. M. Fromager and K. A. Ameur, "Modeling of the self-Q-switching behavior of lasers based on chromium doped active material," Opt. Comm. **191**, 305-314 (2001).
100. N. Passilly, M. Fromager, K. Ait-Ameur, R. Moncorge, J. L. Doualan, A. Hirth, and G. Quarles, "Experimental and theoretical investigation of a rapidly varying nonlinear lensing effect observed in a $Cr^{3+}$: LiSAF laser," J Opt Soc Am B **21**, 531-538 (2004).
101. N. Passilly, E. Haouas, V. Ménard, R. Moncorgé, and K. A¨t-Ameur, "Population lensing effect in Cr:LiSAF probed by Z-scan technique," Opt. Comm. **260**, 703–707 (2006).
102. H. Ogilvy, M. J. Withford, R. P. Mildren, and J. A. Piper, "Investigation of the pump wavelength influence on pulsed laser pumped Alexandrite lasers," Appl. Phys. B **81**, 637-644 (2005).
103. W. Gadomski and B. Ratajska-Gadomska, "Homoclinic orbits and chaos in the vibronic short-cavity standing-wave alexandrite laser," J Opt Soc Am B **17**, 188-197 (2000).
104. W. Gadomski, B. Ratajska-Gadomska, and R. Meucci, "Homoclinic dynamics of the vibronic laser," Chaos Solitons & Fractals **17**, 387-396 (2003).
105. A. Sennaroglu, U. Demirbas, S. Ozharar, and F. Yaman, "Accurate determination of saturation parameters for $Cr^{4+}$-doped solid-state saturable absorbers," Journal of the Optical Society of America B-Optical Physics **23**, 241-249 (2006).
106. J. Xiong, H. Peng, P. Hu, Y. Hang, and L. Zhang, "Optical characterization of $Tm^{3+}$ in $LiYF_4$ and $LiLuF_4$ crystals," Journal of Physics D: Applied Physics **43**, 185402 (2010).
107. B. M. Walsh, N. P. Barnes, M. Petros, J. Yu, and U. N. Singh, "Spectroscopy and modeling of solid state lanthanide lasers: Application to trivalent $Tm^{3+}$ and $Ho^{3+}$ in $YLiF_4$ and $LuLiF_4$," Journal of Applied Physics **95**, 3255-3271 (2004).
108. B. M. Walsh, N. P. Barnes, and B. D. Bartolo, "Branching ratios, cross sections, and radiative lifetimes of rare earth ions in solids: Application to $Tm^{3+}$ and $Ho^{3+}$ ions in $LiYF_4$," J. Appl. Phys. **83**, 2772-2787 (1998).
109. S. A. Payne, L. L. Chase, L. K. Smith, W. L. Kway, and W. F. Krupke, "Infrared Cross-Section Measurements for Crystals Doped with $Er^{3+}$, $Tm^{3+}$, and $Ho^{3+}$," IEEE Journal of Quantum Electronics **QE-28**, 2619-2630 (1992).
110. C. Li, Y. Guyot, C. Linares, R. Moncorgé, and M. Joubert, "Radiative transition probabilities of trivalent rare-earth ions in $LiYF_4$," in *Advanced Solid State Lasers*, (Optical Society of America, 1993), NL7.
111. A. Sennaroglu, *Photonics and laser engineering : principles, devices, and applications* (McGraw-Hill, New York, 2010).

112. A. Martinez, "Spectroscopic characterization of Iron-doped II-VI compounds for laser applications," (University of Alabama, 2015).
113. J. J. Zayhowski and C. Dill, "Diode-pumped passively Q-switiched picosecond microchip lasers," Opt. Lett. **19**, 1427-1429 (1994).
114. B. Braun, F. X. Kartner, U. Keller, J.-P. Meyn, and G. Huber, "Passively Q - switched 180-ps Nd:$LaSc_3(BO_3)_4$ microchip laser," Opt. Lett. **21**, 405-407 (1996).
115. F. X. Kartner, L. R. Brovelli, D. Kopf, M. Kamp, I. Calasso, and U. Keller, "Control of solid state laser dynamics by semiconductor devices," Optical Engineering **34**, 2024-2036 (1995).
116. M. N. Cizmeciyan, J. W. Kim, S. Bae, B. H. Hong, F. Rotermund, and A. Sennaroglu, "Graphene mode-locked femtosecond Cr:ZnSe laser at 2500nm," Opt. Lett. **38**, 341-343 (2013).
117. D. Milam, M. J. Weber, and A. Glass, "Nonlinear refractive index of fluoride crystals," Applied Physics Letters **31**, 822-825 (1977).

## VITA

İsmail Yorulmaz was born in Sivas, on February 1, 1987. He received his B.S. degree in physics from Bilkent University in 2010 and the M.S. degree in materials science and engineering from Koç University in 2012. After graduation, he was admitted to the Ph.D. program of the same field. He is a member of OSA and SPIE. His current research interests include mid-infrared solid-state lasers, diode-pumped solid-state lasers and ultrafast lasers.

**Publications:**

- I. Yorulmaz, E. Beyatli, A. Kurt, A. Sennaroglu, and U. Demirbas, “Efficient and low-threshold Alexandrite laser pumped by a single mode-diode,” Opt. Mater. Express, 4, 776-789 (2014).
- F. Canbaz, I. Yorulmaz, and A. Sennaroglu, "2.3-μm $Tm^{3+}$:YLF laser passively Q-switched with a $Cr^{2+}$:ZnSe saturable absorber," Opt. Lett.42, 1656-1659 (2017).
- F. Canbaz, I. Yorulmaz, and A. Sennaroglu, " Kerr-lens mode-locked 2.3-μm $Tm^{3+}$:YLF laser: a new source of femtosecond pulses in the mid infrared," Opt. Lett. 42, 3964-3967 (2017).
- I. Yorulmaz, and A. Sennaroglu, "Low threshold diode pumped 2.3-μm $Tm^{3+}$:YLF lasers," (submitted).

**Patent:**

- B. Alaca, Y. Leblebici, I. Yorulmaz, Y. Kilinc, B. Aksoy, “Nanomechanical resonator array and production method thereof” US 9,413,333 (EP2987239, WO2014169960), Aug. 2016.

**Proceedings:**

- E. Beyatli, I. Baali, I. Yorulmaz, A. Kurt, B. Sumpf, G. Erbert, A. Sennaroglu, A. Leitenstorfer, and U. Demirbas, "Efficient and Low-Threshold Alexandrite Lasers Pumped by High-Brightness Diodes," in ASSL 2013, Paris, France.

- Ferda Canbaz, Ismail Yorulmaz, and Alphan Sennaroglu, “Passive Q-Switching of a $Tm^{3+}$:YLF Laser at 2.3 μm with a $Cr^{2+}$:ZnSe Saturable Absorber” in ASSL 2017, Nagoya, Japan.